A numerical study of gas explosion with progressive venting in a utility tunnel

Di Chen[a, b], Chengqing Wu[a], Jun Li[a], Kexi Liao[b]

[a] *School of Civil and Environmental Engineering, University of Technology Sydney, Sydney, NSW, 2007, Australia*

[b] *School of Oil & Natural Gas Engineering, Southwest Petroleum University, Chengdu, Sichuan, 610500, China*

Keywords: CFD; gas explosion; progressive venting; moving obstacle; artificial neural network

Abstract

A numerical model of a progressive vented gas explosion is presented. A CFD tool in combination with correlation analysis and an artificial neural network (ANN) were utilized to establish and refine the numerical model. The experimental results of 44 fixed vented gas explosions and one progressive vented gas explosion with moving obstacles were used to validate the numerical accuracy. The results indicated that the method to estimate the activation pressure of the pressure relief panels for a fixed vented gas explosion achieved a lower overpressure prediction compared to that for a progressive vented gas explosion. The progressive venting procedure was modelled by two-layer pressure relief panels with the upper layer having activation pressures with a linear ascent trend. The vents on the tunnel had an insignificant impact on the explosion load after being lifted over the tunnel top, and their falling process was unnecessary to be modelled. A non-negligible impact of the obstacles inside the tunnel on the flow field upon being pushed away from their initial positions was demonstrated. By employing an ANN, the critical parameters in the numerical model were determined, which were used to accurately replicate the experimental results. The findings clarified a revenue for the modeling of a progressive vented gas explosion as well as some shortcomings of the CFD tool.

1 Introduction

Natural gas is a widely used energy source in daily life and industrial production. In 2020, natural gas contributed 24.7% of the total energy consumption globally, reaching a record high even though the pandemic reduced energy consumption (BP 2021). With ever-increasing popularity, safety issues in the natural gas transportation, storage and end-use

are attracting increasingly more attention. In fact, natural gas explosion accidents are not uncommon in the world and may cause enormous casualties and economic losses (Cheng et al., 2015).

Venting of a gas explosion represents an effective way to mitigate the blast effects on human beings and structures (Chmielewski and Bąk, 2021; Li and Chen, 2014). Carefully designed venting devices ensure the reduction in blast pressure. For example, the maximum overpressure of approximately 2.2 bars was observed in a series of natural gas explosion tests conducted in a 4.5m×4.5m×9m container with vent openings (Tomlin et al., 2015). By comparison, the maximum pressure of 7.8 bars was captured in a totally confined 0.12 m^3 spherical container (Nishimura et al., 2013).

Vented gas explosions have been studied experimentally and numerically. An experiment is the most direct and reliable way to investigate governing factors affecting the vented gas explosion characteristics. Cooper et al. (Cooper et al., 1986) performed a series of gas explosion tests in near-cubic enclosures with pressure relief panels, and 4 evident pressure peaks were identified. As shown in Fig. 1, P_1 was generated prior to the opening of the relief panel which was attributed to the gas expansion in a confined reaction vessel owing to combustion. After the relief panel was broken, a certain amount of unburned methane-air mixture was expelled from the container and continued combusting outside the vessel, which resulted in a sharp increment in the internal pressure known as P_2. P_3 occurred when the flame occupied the largest space in the vessel. The peak pressure P_4 was generated by the coupling of the combustion process with acoustic modes of the vessel. It was reported that the acoustically enhanced P_4 would not be of importance in a wide range of practical situations. Park et al. (Park et al., 2008) examined the flame interaction with different obstacle arrangements and pointed out that a higher overpressure would be induced by stronger turbulence caused by obstacles. Kasmani et al. (Kasmani et al., 2013) conducted a series of gas explosion tests in a cylindrical vessel connected with a vent duct to explore the influence of vent burst pressure and ignition location on overpressures, and concluded that the vent burst pressure was complex and a non-linear effect was observed which did not coincide with the design standard of NFPA 68 (National Fire Protection Association, 2007). Tomlin et al. (Tomlin et al., 2015) conducted 38 vented gas explosion tests in a 182 m^3 explosion chamber with different vent and congestion situations, indicating that a damaging overpressure could be derived even in empty enclosures as the venting size was insufficient and the presence of obstacles enhanced the overpressure significantly. Guo et al. (Guo et al., 2016) studied the effect of the activation pressure of vent panels on the explosion load in a cylindrical vessel, and demonstrated that the maximum overpressure increased approximately linear with the activation pressure of vent panels. Li et al. (Li and Hao, 2018, 2019; Li et al., 2017) conducted a series of in-

situ tests in large-scale storage tanks to explore the effect of the enclosure scale, vent condition and gas concentration on the pressure load characteristics. Li et al. ([a]Li et al., 2017; [b]Li et al., 2019; [c]Li et al., 2017; [d]Li et al., 2017) investigated the effect of gas concentration and vent opening characteristics both on load characteristics and structural response through full-scale in-situ tests, and concluded that the design guides (NFPA68 (Association, 2007) and EN 14994 (European Committee for Standardization, 2007)) and the TNT-equivalency method suggested by CCPS (Kumar, 1994) as well as UFC3-340-02 (Department Of Defense, 2008) gave very conservative load predictions. Yu et al. (Yu et al., 2017) examined the effect of the side venting position in a pipeline on methane/air explosions and confirmed that the overpressure development was affected by the interaction of side and end vents. Xing et al. (Xing et al., 2020) researched into the influence of vent area and ignition position on overpressure oscillations in a large L/D ration duct, and indicated that a violent pressure oscillation occurred when the methane concentration was between 9.5 and 12.0 vol. % with small vent area. Wang et al. (Wang et al., 2022) captured the internal and external overpressures from vented hydrogen deflagration in a rectangular tube with different vent coefficients, and implied that the maximum internal overpressure was dominated by the external explosion in the case of a large vent coefficient. To summarize, there are a range of factors affecting the load characteristics and the subsequent structural response in a vented gas explosion. For example, the enclosure size and shape, vent size and activation pressure, ignition energy and location, obstacles and their configuration, mixture property, initial turbulence, temperature, and humidity all affect the load characteristics.

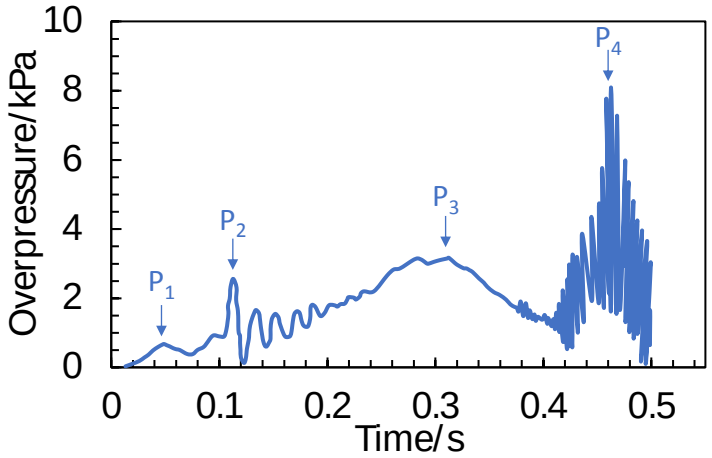

Fig. 1. A typical pressure history curve of vented gas explosion in a near-cubic vessel (Cooper et al., 1986)

Large-scale gas explosion tests are often prohibitive due to the high cost and long preparation time. With the advancement in computational mechanics, it has become possible to model complex gas combustion and explosion scenarios. For instance, the widely-recognized CFD tool FLACS, verified by a wide variety of gas explosion tests

(Arntzen, 1998; Bleyer et al., 2012; Salaun et al., 2016; Vyazmina and Jallais, 2016), is expected to yield acceptable accuracy of estimations in various gas explosion scenarios, with confinement and congestion effects at different scales. Bakke et al. (Bakke et al., 2004) utilized FLACS to explore the protection efficiency of explosion relief panels in a full-scale offshore module. Pedersen et al. (Pedersen and Middha, 2012) simulated a vented gas explosion scenario in a 64 m^3 explosion chamber using FLACS and indicated that the simulation results agreed well with experimental data and could be used for evaluating pressure loads for vented explosions. Li et al. (Li et al., 2017) employed the same CFD tool to simulate vented methane-air explosions in cylindrical enclosures, and both the peak overpressures and pressure history curves were well predicted by FLACS. Li and Hao (Li and Hao, 2018) simulated the inner and outer pressure load from a vented gas explosion tank and clarified the shortcomings of FLACS in far-field pressure prediction. Zhu et al. (Zhu et al., 2020) utilized FLACS to investigate the overpressure of methane-air explosions in a long tunnel and demonstrated that reducing the confinement was helpful to mitigate accident consequences. Lucas et al. (Lucas et al., 2021) modeled vented hydrogen explosions in 20-foot shipping containers by utilizing FLACS and concluded that this CFD tool achieved reasonable accuracy in hydrogen release, dispersion and explosion scenarios.

All vented gas explosion scenarios mentioned above had up to several vent openings which were opened in very short time intervals. This type of gas explosion, termed as a fixed vented gas explosion in this study, happened in spaces where the length, width, and height were of the same order of magnitude, and the pressure load was roughly even distributed ([d]Li et al., 2017) and sharply declined after the vent devices failure. However, in recent years, there were gas explosion accidents with much more vent openings that were damaged sequentially in a longer duration. A tragedy happened in Qingdao in 2013, which killed 62 and injured 136, was ascribed to a crude oil vapor explosion in storm drains. About 5 km of drains' covered by reinforced concrete slabs was lifted gradually in this accident (Zhu et al., 2015). Another gas explosion accident in the Kaohsiung City of China, that resulted in 32 fatalities and 321 injuries, occurred in an underground trench which blew out around 400 m of the road above the ground (Yang et al., 2016). In this kind of gas explosion, which was termed as a progressive vented gas explosion in this study, the damage process continued to propagate even though part of the confined space had been broken and the vent opening was already formed, indicating that the pressure did not decrease upon the inception of the venting process. The progressive gas explosion usually appeared in quite long confined spaces, which is quite common in city's gas supply systems. As many gas pipelines are going through underground utility tunnels (Meng et al., 2021), it is very challenging to replicate the progressive vented process in laboratory work.

In the past few years, 4 progressive vented gas explosion tests were conducted and reported in literature in 12 m and 20 m utility tunnels (Meng et al., 2020; Meng et al., 2020; Meng et al., 2021; Yang et al., 2021). This study is an extension of those studies to model the progressive vented gas explosion process by CFD simulations. First, the fixed vented gas explosions were modeled with FLACS to achieve grid convergence. Then, the numerical model of a progressive vented gas explosion with moving obstacles was established. Due to the complexity of the boundary conditions in the numerical model, an ANN-based tool was utilized to determine the key parameters so as to save computational time involved in pure numerical simulation. The experimental data were employed to ensure the accuracy of the numerical output. The results of this study promote the application of the numerical modeling of the progressive vented gas explosion in exploring gas explosion accidents and preventing their occurrence. Some shortcomings of the CFD tool FLACS were also clarified.

2 Numerical model

The CFD code FLACS was utilized to model the vented gas explosions in this study. It solves the compressible conservation equations and Reynolds Navier-Stokes equations on a 3D Cartesian grid using a finite volume method (Gexcon, 2019). Turbulence is modeled by the two-equation k-ε model (Launder and Spalding, 1974). The interaction of the reactive flow with the surrounding geometry is taken into account through a distributed porosity concept, and the k-ε model is modified to capture the impact of turbulence production from the subgrid geometry (Pedersen et al., 2013). The numerical flame is modeled by 3-5 control volumes using a so-called β-model (Arntzen, 1998).

With FLACS, objects with small displacement are modelled as rigid bodies. For those which have significant movement during the explosion process, such as moving obstacles and venting panels, FLACS can model them as pressure relief panels. In FLACS, the pressure relief panel is a 2-D rectangle with a predefined weight to imitate the inertia. By modifying the porosity in the region where the pressure relief panel is positioned, the movement of objects is simulated. The panel yield duration is determined by the panel weight and subgrid as well as the force applied to the panel (Gexcon, 2019). As shown in Table 1, several parameters are used to control the opening behavior of the pressure relief panel. There are several types of pressure relief panels provided by FLACS to simulate different deformation behavior of moving objects. For example, POPOUT is used to simulate a panel with linear displacement, whereas HINGED is utilized for rotational movement. In this study, the type of POPOUT was employed.

Table 1 Parameters controlling the opening behavior of pressure relief panel (Gexcon, 2019)

Parameter	Unit	Description
Position	m	Cartesian coordinates of the corner of the panel.
Size	m	The dimension in each of the axis directions.
Panel type	-	The type of panel to emulate different deformation behavior of moving objects. The most used types are POPOUT and HINGED.
Opening pressure differences	bar	A given value that the panel starts to yield when the net pressure over the panel exceeds it.
Initial and finial porosity	-	The initial and final porosity of the panel before and after yielding.
Weight	kg/m^2	The per unit area mass of the panel.
Drag coefficient	-	The ratio of "drag force/dynamic pressure". If the Reynolds number is high, such as in the explosion process, the drag coefficient is constant. A value 2.0 is set by the FLACS code as a fixed preset value for the panel types POPOUT and HINGE, so users do not need to input its value.
Maximum travel distance	m	The maximum travel distance is the smallest distance from the initial position of the panel to the position where the yielded panel no longer affects significantly the effective area-porosity at the initial position of the panel. For the panel types of POPOUT and HINGRD, its value is calculated from the panel subsizes, so users do not have to input its value.
Panel subsizes	m	The panel subesizes are the sizes of sub panel. The panel types of POPOUT and HINGRD are assumed to consist of sub-panels mounted on a frame.

3 Numerical simulation of fixed vented gas explosion

3.1 Experimental setup

The full-scale vented gas explosion tests with different methane concentrations, vent window designs and masonry wall designs conducted in a reinforced chamber with the internal dimensions of 3.0m×2.0m×2.0m ([a]Li et al., 2017; [b]Li et al., 2019; [c]Li et al., 2017; [d]Li et al., 2017) were taken as the numerical references. The experimental setup is presented in Fig. 2. A total of 44 overpressure history curves were collected from literature studies. Either the masonry wall or the vent window, or both of them collapsed in each test. The venting position collapsed almost at the same time, and the overpressure declined sharply following on the collapse of the masonry wall or the vent window. Details of the 44 experimental tests are listed in Table 2.

The chamber was filled with a homogeneous methane-air mixture. After the concentration of methane in the chamber reached the desired level, the fuel was ignited at the center of the chamber. The history curves obtained from each test displayed one, two or three distinct pressure peaks defined by Cooper et al. (Cooper et al., 1986) as P_1, P_2, P_3 and P_4 that are driven by different mechanisms.

Table 2 An overview of the 44 tests ([a]Li et al., 2017; [b]Li et al., 2019; [c]Li et al., 2017; [d]Li et al., 2017)

NO.	Test NO.	Masonry type	Weight kg/m^2	Boundary	Methane concentration %	Vent cover	Weight kg/m^2	P_1 kPa	Wall status	Vent window status
1	1				12.5	4 mm glass		10.76	survived	
2	2	S1	276	One-way	7.5	4 mm glass	10	13.8	survived	collapsed
3	3				7.5	4 mm glass		6.56	collapsed	
4	4	S2	276	One-way	12.5	4 mm glass	10	7.31	survived	collapsed
5	5				7.5	4 mm glass		7.56	collapsed	
6	6				12.5	4 mm glass	10	9.96	survived	
7	7	S3	276	Two-way	12.5	8 mm glass	20	39.29	survived	collapsed
8	8				7.5	4 mm glass	10	9.67	survived	
9	9				9.5	8 mm glass	20	146.5	collapsed	
10	10				11.5	6 μm film	5.5×10^{-3}	3.64	survived	
11	11	S4	132	One-way	6.5	4 mm glass	10	7.78	survived	collapsed
12	12				6.5	4 mm glass	10	10.13	collapsed	
13	13				12.5	6 μm film	5.5×10^{-3}	2.73	survived	
14	14	S5	132	One-way	12.5	4 mm glass	10	9.96	survived	collapsed
15	15				9.5	1.5 μm film	1.4×10^{-3}	1.53	collapsed	
16	16	S6	132	Two-way	≈8.5	6 μm film	5.5×10^{-3}	1.89	collapsed	collapsed
17	1				11.5	6 μm film	5.5×10^{-3}	3.77	survived	
18	2	S7	132	One-way	6.5	4 mm glass	10	7.83	survived	collapsed
19	3				6.5	4 mm glass	10	10.12	collapsed	
20	4				6.5	4 mm glass	10	10.32	survived	
21	5	S8	132	One-way	12.5	10 mm glass	25	32.79	survived	collapsed
22	6				12.5	12 mm glass	30	46.16	collapsed	
23	7				6.5	4 mm glass	10	8.73	survived	
24	8	S9	132	One-way	6.5	5 mm glass	12.5	20.93	survived	collapsed
25	9				12.5	10 mm glass	25	40.45	collapsed	
26	1				12.5	6 μm film	5.5×10^{-3}	2.91	survived	
27	2	S10	75	Two-way	12.5	4 mm glass	10	13.25	survived	collapsed
28	3				9.5	1.5 μm film	1.4×10^{-3}	85.88	collapsed	
29	4				12.5	6 μm film	5.5×10^{-3}	2.96	survived	collapsed
30	5	S11	75	Two-way	12.5	4 mm glass	10	9.27	survived	collapsed
31	6				12.5	5 mm glass	12.5	21.26	survived	collapsed
32	7				9.5	12 mm glass	30	43.17	collapsed	survived
33	8				12.5	6 μm film	5.5×10^{-3}	3.11	survived	collapsed
34	9	S12	75	Two-way	12.5	4 mm glass	10	7.57	survived	collapsed
35	10				7.5	12 mm glass	30	32.3	collapsed	survived

NO.	Test NO.	Masonry type	Weight kg/m^2	Boundary	Methane concentration %	Vent cover	Weight kg/m^2	P_1 kPa	Wall status	Vent window status
36	1				12.5	1.5 μm film	1.4×10^{-3}	0.74	survived	collapsed
37	2	S13	75	One-way	12.5	6 μm film	5.5×10^{-3}	3.84	survived	collapsed
38	3				12.5	4 mm glass	10	5.15	collapsed	survived
39	4				12.5	1.5 μm film	1.4×10^{-3}	0.37	survived	collapsed
40	5	S14	75	One-way	12.5	6 μm film	5.5×10^{-3}	2.75	survived	collapsed
41	6				9.5	12 mm glass	30	13.61	collapsed	survived
42	7				12.5	6 μm film	5.5×10^{-3}	2.91	survived	
43	8	S15	75	Two-way	12.5	4 mm glass	10	13.25	survived	collapsed
44	9				9.5	1.5 μm film	1.4×10^{-3}	1.23	collapsed	

Note: The boundary condition of one-way denotes the masonry wall was constructed with the right and left boundaries isolated from the RC frames by using plastic film. The two-way boundary denotes the masonry wall was bolted onto the RC frames along the left and right boundaries by using steel bars with an equal space of 50 cm. S1, S2, S3, S4, S5 and S6 masonry walls were all fabricated by unreinforced clay brick masonry. S1, S2 and S3 were 240 mm in wall thickness. S4, S5 and S6 were 115 mm in wall thickness. S7, S8 and S9 were constructed by clay bricks with the thickness of 115 mm. S7 was not strengthened. S8 was retrofitted by distributed carbon fiber reinforced polymer (CFRP). S9 was strengthened by concentrated CFRP. S10, S11 and S12 were fabricated by autoclaved aerated concrete (AAC) with the thickness of 120 mm. S10 was unstrengthened. S11 was rear-face strengthened by basalt fiber reinforced polymer (BFRP), and S12 was front-face strengthened by BFRP. S13, S14 and S15 were made of AAC with the thickness of 120 mm, and no strengthened method was used.

3.2 Numerical model

Fig. 2 shows the experiment and FLACS 3D geometries. The vent windows and masonry walls were modeled by the pressure relief panels. For the vent windows or masonry walls that did not experience collapse, the activation pressure was set as 999 bars, so the panels did not yield during the explosion process. For masonry walls or/and vent windows that experienced collapse deformation, the activation pressure of the panel was equal to P_1, as P_1 was always associated with the removal of the explosion relief vent panels and its magnitude was identical to or slightly greater than the activation pressure of the vent panel (Pedersen et al., 2013).

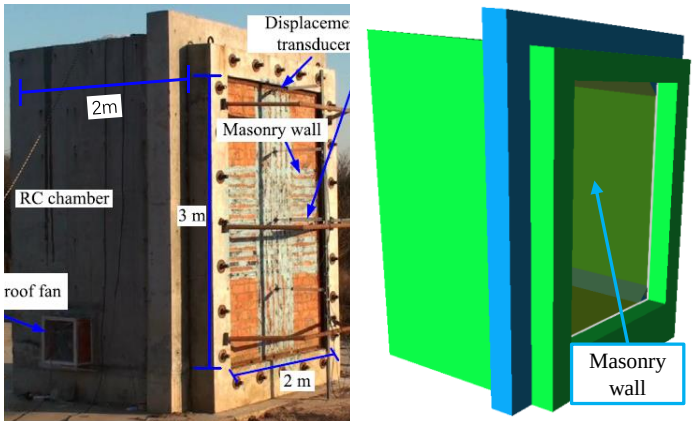

(a) Side view

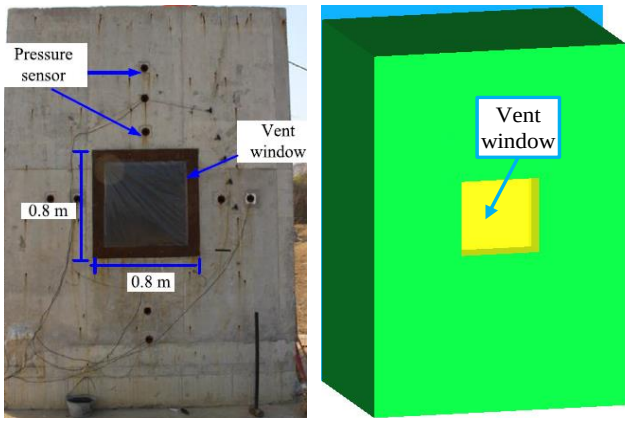

(b) Back view

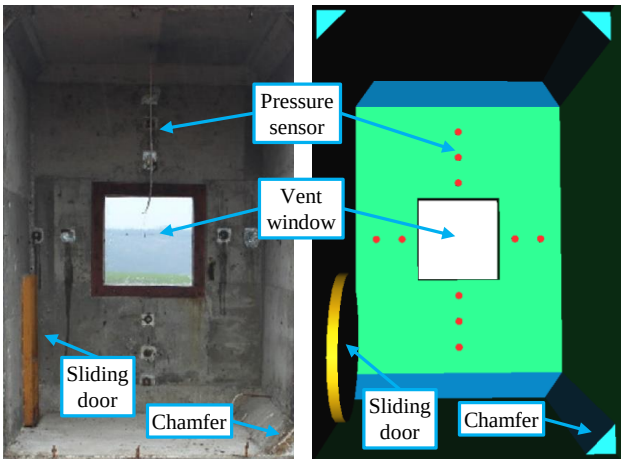

(c) Internal view

Fig. 2. Details of the experiment ([b]Li et al., 2019) (left) and FLACS 3D geometries (right).

For all simulations, the initial pressure and temperature were 1 bar and 20 ℃, respectively. All the objects excluding the vent window and collapsed masonry wall were modeled as rigid. The boundary condition of Z^- was EULER to model the reflection effect of the ground, whereas the other 5 directions of boundary conditions were PLANE_WAVE to eliminate the pressure wave reflection. As shown in Fig. 3, grid cells in the chamber region were modeled cubically. To reduce boundary influences and computational difficulty, the grid region was stretched to 2 times larger in the X^+ and X^- direction, 4 times in the Z^+ direction and 10 times in the Y^+ (vent) direction. For the scenarios where the masonry walls experienced collapse, Y^- was also extended to 10 times larger. The percentage difference of the grid was retained below 30%. CFLC and CFLV, which were used for controlling the time step, were set as 5 and 0.5 (Gexcon, 2019).

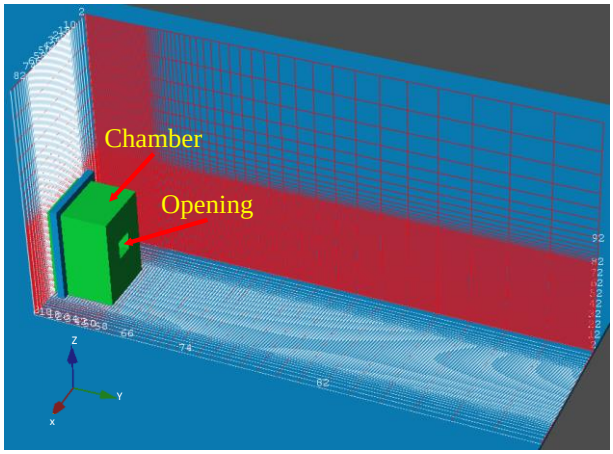

Fig. 3. Computational domain for the chamber gas explosion.

3. 3 Grid independent study

A grid resolution of 10 cm, 5 cm and 4 cm in the chamber region was tested to explore the grid independence. The simulation parameters were set in line with Test 2 conducted by Li et al. ([b]Li et al., 2019). The simulation was performed on a computer with the CPU

of Intel i9-10900 5.2 GHz, and the memory size of 32 GB. A single core was used for each case.

As shown in Fig.4, only P_1 was captured in this experiment, since the pressure curve presented one dominant peak. A grid resolution of 5 cm was necessary since a grid resolution of 10 cm produced a slower rate of pressure rise. The results produced by the 4 cm grid did not show a significant difference with 5 cm resolution. Table 3 presents more details of the results from the different grid sizes. The computational time of the 4 cm grid was about 2 times longer than that of the 5 cm grid size. At the same time, owing to the typical treatment between the propagation of the reacting zone and the flow equations, smaller grid sizes may not necessarily achieve better results. For a grid size of 1-2 cm or less, the subgrid model for premixed combustion was not applicable and the burning velocities tended to be severely overpredicted (Gexcon, 2019). Thus, a 5 cm grid size in the fuel region was employed throughout the study.

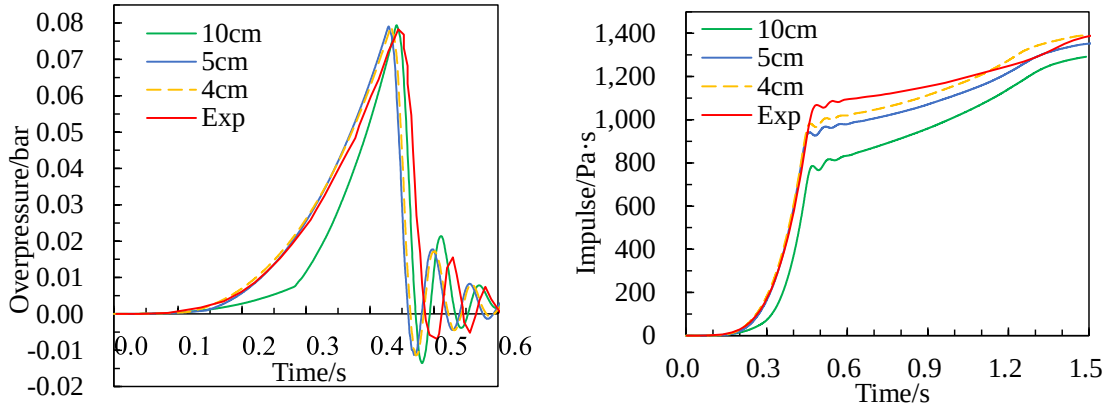

(a) Overpressure history curve (b) Impulse history curve

Fig. 4. Grid cell size dependence of the numerical results ([b]Li et al., 2019).

Table 3 Grid cell size dependence and comparison between numerical and experimental results

Grid size /cm	10	5	4	Experimental value
Peak pressure/kPa	7.94	7.91	7.91	7.83
Error/%	1.40%	1.02%	1.02%	/
Peak impulse/Pa·s	1291	1355	1368	1430
Error/%	-9.72%	-5.24%	-4.34%	/
Cell number	13.9×10^4	72.3×10^4	123.4×10^4	/
Computational time/h	0.61	7.31	15.26	/

3.4 Experimental and numerical result comparison

Up to 3 pressure peaks were captured in each test. As shown in Fig. 5, P_1, P_2 and P_3 were reproduced numerically, and the numerical and experimental curves approximately coincided with each other. However, the model did not yield P_4 generated from the interaction between the flame and acoustic wave (Cooper et al., 1986) as the flame-acoustic interaction is not modeled (Pedersen and Middha, 2012).

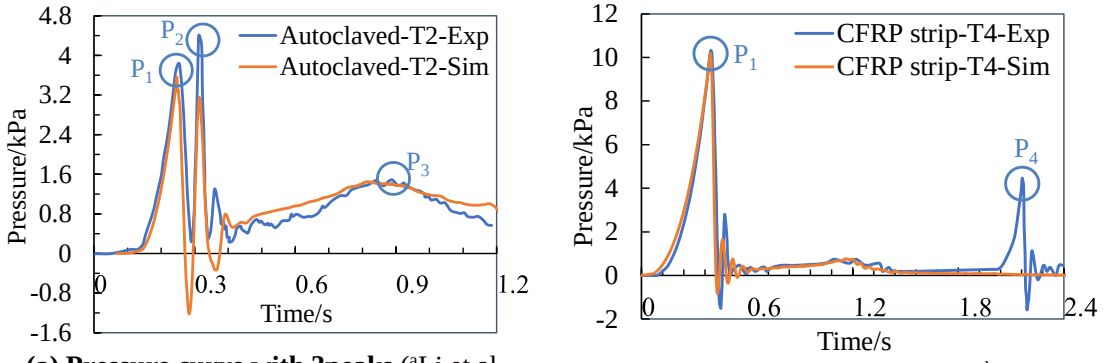

(a) Pressure curve with 3peaks ([a]Li et al., 2017) **(b) Pressure curves with 2 peaks** ([b]Li et al., 2019)

Fig. 5. Overpressure history comparison of multiple overpressure peak curves.

Fig. 6 displays the 44 respective peaks (P_1, P_2 and P_3) collected from literature and compared with the numerical results. The findings revealed that FLACS predicted P_1 accurately within the error of 30%. By comparison, the numerical results of P_2 and P_3 were less accurate.

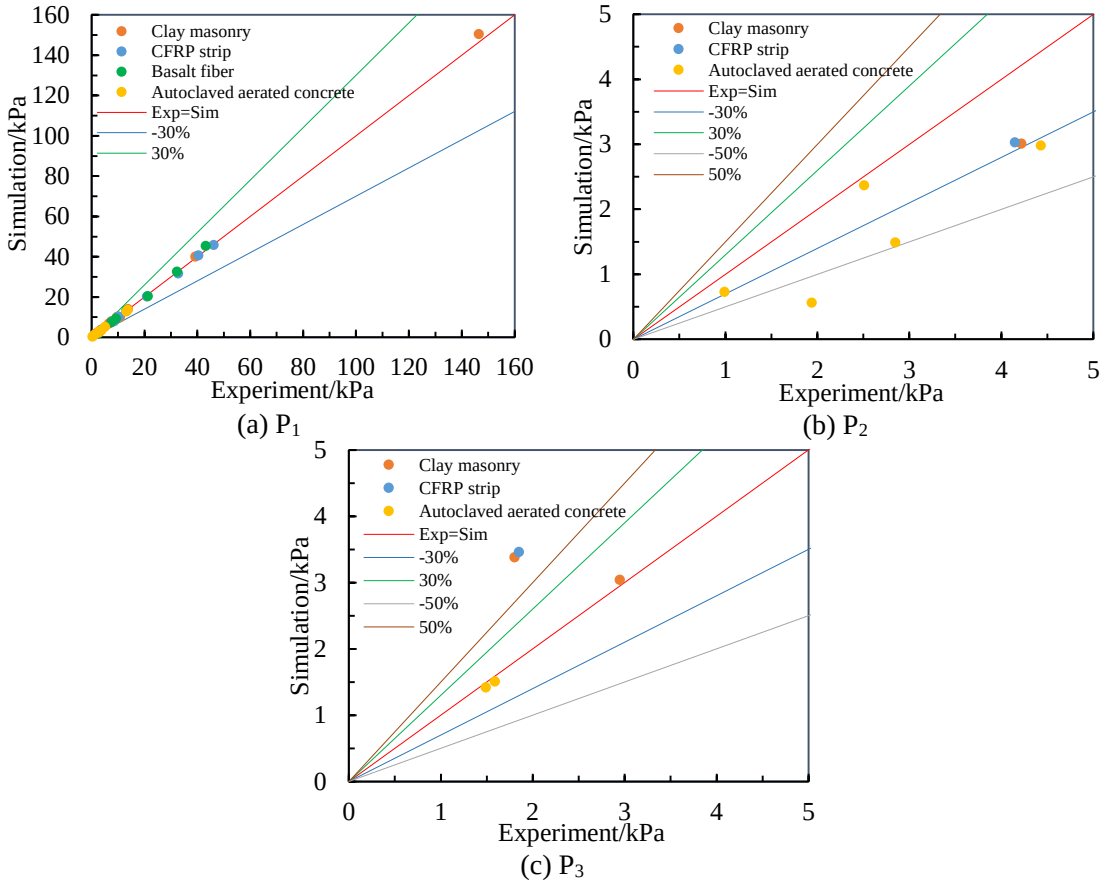

(a) P_1 (b) P_2 (c) P_3

Fig. 6. Experimental and numerical results of overpressure peaks ([a]Li et al., 2017; [b]Li et al., 2019; [c]Li et al., 2017; [d]Li et al., 2017).

The difference between the numerical and experimental results comes from both experimental and numerical aspects. The experimental uncertainty is always existing and can be up to ±50% for repeated tests in vented gas explosion tests (Pedersen and Middha,

2012). As mentioned before, the magnitude of P_1 was identical to or slightly greater than the activation pressure of the vent panel, and P_1 was set as the activation pressure in the numerical model, explaining why P_1 was more accurate compared to P_2 and P_3. Also, FLACS uses a simplified method to model the process of the removal of vent devices. FLACS changes the porosity where the panel is occupied initially but does not trace the movement of the panel. This simplification does not influence P_1 too much as it occurs prior to the panel failure. But this simplification will have a more visual impact on P_2 and P_3 owing to their occurrence after panel failure.

4 Numerical simulation of progressive vented gas explosion

4.1 Experimental setup

A series of full-scale gas explosion tests in a buried tunnel with progressive vent openings and moving obstacles were performed (Meng et al., 2020; Meng et al., 2021; Yang et al., 2021). In this study, the experimental results from Yang's study were selected and compared numerically.

As shown in Fig. 7, the experiment was conducted in a tunnel with dimensions of 0.6 m deep, 1.6 m wide and 20 m long. Because the length of the tunnel was significantly larger than that of depth and width, the pressure load in the tunnel was uneven and the venting covers over the tunnel were lifted one by one during the experiment. The wooden and steel obstacles were placed at the bottom of the tunnel with a spacing of 1 m to increase the turbulence and hence boost the overpressure. The concrete slab specimens were fully constrained by metal fixings at one end of the tunnel away from the ignition point. Except for the concrete slabs, the remaining top cover slabs were made of steel, which were supported by the tunnel and fixed by sandbags. 420 sandbags weighing 25 kg each were evenly placed on the steel slabs. Furthermore, the steel slabs were connected using a square steel tube. All the gaps among the slabs were filled with expandable foam to seal the tunnel. The concentration of methane was 9.5%, and the ignition point was at the opposite end of the concrete slab specimens.

To model aforementioned experimental scenario, the main challenge came from the multi-vent openings along the tunnel length and the moving obstacles inside the tunnel. The first challenge was to model the lifting process of the steel slabs. Unlike a fixed vented gas explosion in which the venting panels damaged at relatively constant pressure and short duration, the relief pressure for the progressive vented explosion in the experimental scenario was more difficult to estimate as the expandable foam among the gaps and the square tube connected with the steel slabs gave much uncertainty. The steel slabs were lifted one by one, indicating that it was not a fixed pressure when the slabs

were blown up. What is more, during the process of lifting from the tunnel top, the steel slabs still contributed to the confined space of the tunnel, so it was unclear whether the period after the steel slabs were lifted away from the tunnel top should be taken into consideration. Also, to what extent the falling process of the steel slabs affected the explosion process was unclear. Another difficulty was modeling the moving obstacles inside the tunnel. These obstacles should be taken into account at the early stage of the explosion process but could be ignored when the explosion process developed into a certain phase when these obstacles were displaced to one end of the tunnel or even blown out of the tunnel. CFD simulations in combination with correlation analysis and an artificial neural network (ANN) were utilized to overcome these challenges.

4.2 Modelling progressive vented gas explosion

Typically, the activation pressure of the pressure relief panels was predetermined as the value when the panel started to be removed. A numerical model was established to verify its applicability for a progressive vented gas explosion.

4.2.1 Numerical model

As shown in Fig. 7, the tunnel walls, concrete specimen covers and the tube were modeled as rigid bodies. The obstacles inside the tunnel were modeled as pressure relief panels having the identical width and height as the real obstacles. The computational domain was stretched to reduce boundary influence.

The activation pressure of the steel slabs and the obstacles' activation pressure were the critical parameters in the numerical model. The initial activation pressures of the obstacles were estimated as:

$$x_{1(2)}\, s_{1(2)} > \mu_{1(2)}{}' N_{1(2)} \tag{2}$$

where x_1 is the activation pressure of the wooden obstacles; x_2 is the activation pressure of the steel obstacles; $s_{1(2)}$ is the area of the pressure relief panels, m^2; $\mu_{1(2)}$ is the friction coefficient between the wooden (steel) and the tunnel bottom; $N_{1(2)}$ is the gravity of each wooden (steel) obstacle, N.

The densities of wooden and steel were 600 kg/m^3 and 7850 kg/m^3, respectively, and the volumes of each wooden and steel obstacle were 2.88×10^{-3} m^3 and 6.72×10^{-4} m^3, so N_1 and N_2 were 19.6 N and 51.7 N. μ_1 and μ_2 were estimated as 0.8 and 0.65, respectively (Jaaranen and Fink, 2020; Rabbat et al., 1985). Hence, the values of x_1 and x_2 were estimated as 4.7×10^{-4} bar and 2.5×10^{-3} bar, respectively.

When the inner pressure exceeded the gravity force of the steel slabs, the slabs over the tunnel started to move. This inner pressure was denoted by x_3 here. The weight of each slab (including the weight of sandbags above it) was around 252.4 kg. Hence, x_3 was estimated to be 3.9×10^{-2} bar. There were expandable foam and rubber among the steel slab gaps, and square steel tubes connecting the steel plates together, which provided additional drag forces to the steel slabs, so x_3 must be greater than 3.9×10^{-2} bar, here x_3 was multiplied by 1.5, and the final value for x_3 was 5.8×10^{-2} bar.

(a) Arrangement of obstacles

(b) Experimental site setup

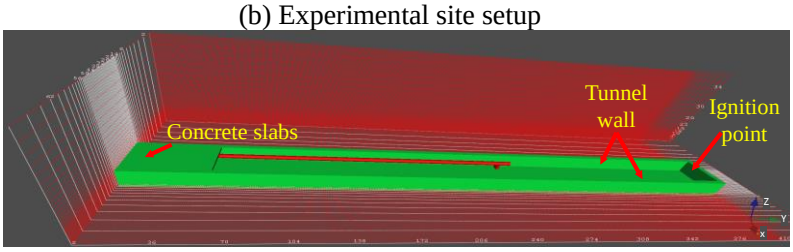

(c) Geometry model and computational grid

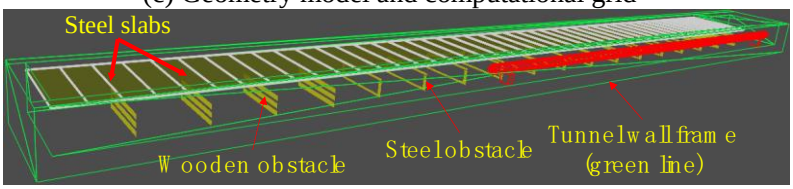

(d) The pressure relief panels' position

Fig.7 Details of experimental setup and numerical geometry

4.2.2 Numerical result

The predicted pressure curve is presented in Fig. 8. The peak pressures at positions #1 and #2 were 0.088 bar and 0.086 bar, respectively, which were far lower than the experimental values of 3.15 bar and 2.37 bar. The pressure duration was also much shorter than the experimental one (as shown in Fig. 10). The results revealed that the typical method suitable for modeling the fixed vented gas explosion is inappropriate for a progressive vented gas explosion. The model only changes the porosity in the region where the pressure relief panel is positioned. Consequently, the tunnel began to turn into an open space when the inner overpressure overcame the gravity of the steel slabs. However, in the real situation, when the inner overpressure overcame the gravity of the steel slabs, the slabs just initiated the movement with an increasing velocity from 0 m/s. There was still 0.1 m to go before the slabs were lifted over the tunnel top. During this period, the steel slabs and the tunnel wall altogether could still be considered as a confined space, and the overpressure would increase dramatically in such a space. Therefore, the typical method used to model the progressive vented gas explosion caused the premature opening of the tunnel cover and resulted in a lower overpressure assessment.

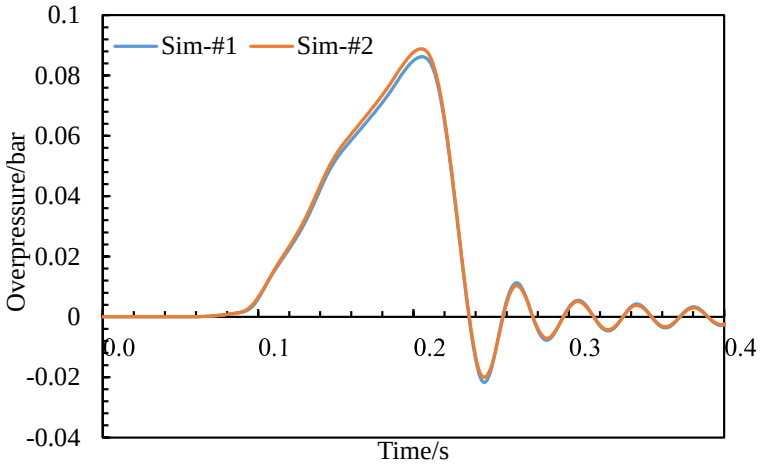

Fig. 8. The numerical result based on the typical method

4.3 The modified method in modelling progressive vented gas explosion

4.3.1 Numerical model

Based on the high-speed video images that recorded the experimental process, the steel slabs were lifted to about 0.8 m above the tunnel top. The high-speed video images also showed that there was a persistent interaction between the steel slabs and the flame when the steel slabs were lifting, indicating that the pressure relief process might last for the whole lifting process of the steel slabs. Hence, the steel slab cover was modeled as 10 layers of pressure relief panels with the top layer 0.8 m away from the tunnel top to simulate the dynamic lifting process of the steel slabs (Fig. 9). Each layer consisted of 44 panels with dimensions of 0.4 m wide and 1.6 m long which was identical to the real steel slabs. The distance between 2 layers of panels was set as 0.1 m. The bottom 2 layers of pressure relief panels were inside the tunnel as the upper tunnel wall from 0.6 m to 0.7 m was used to place the concrete specimens and steel slabs. The overall number of pressure relief panels in the established numerical model was 506.

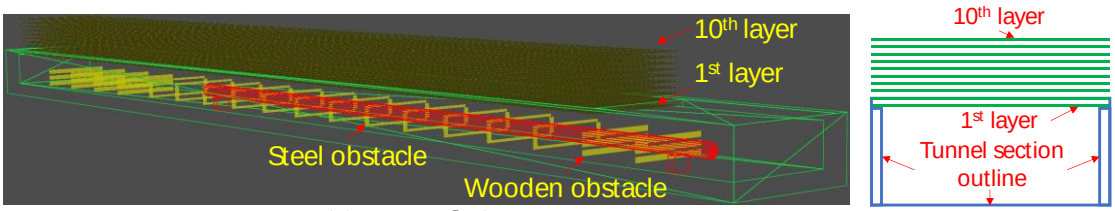

(a) General view **(b) Section view**

Fig. 9. Details of the pressure relief panels.

4.3.2 Mathematical model and solving procedure

For the numerical model, the initial and boundary conditions need to be known. A few parameters, such as the layout of the tunnel, the weight of obstacles, steel slabs and sandbags, the methane concentration, and the initial temperature could be obtained directly from the experimental setup. The main challenge was to determine the activation pressure of the steel slabs over the tunnel and the obstacles' activation pressure. Numerous simulations might be needed to replicate the experimental results, as 506 activation pressures of pressure relief panels were needed to be determined in theory. Hence, an ANN-based tool was utilized to substitute the simulation process with limited numerical data as the training data aiming to save a large amount of computational time involved in pure numerical simulation.

A mathematical model involving the activation pressures was established to help implement the ANN tool. To describe and solve the model efficiently, assumptions were made as follows: (1) Each wooden and steel obstacle had the same activation pressure, respectively. (2) The steel slabs only moved in the vertical direction, and the rotation of each slab was neglected. (3) The tunnel walls and concrete slabs were considered as rigid bodies. (4) It was the ascending, not the descending process of the steel slabs that dominated the pressure characteristics. Excluding the foregoing 4 assumptions, each layer of pressure relief panels above the tunnel having the identical activation pressure was assumed at first. Based on these assumptions, the problem can be characterized as:

$$f(x_1, x_2, \ldots, x_{12})=(y_1, y_2) \quad (1)$$

where x_1 is the activation pressure of wooden obstacles, x_2 is the activation pressure of steel obstacles, x_3 to x_{12} are the activation pressures from the 1st to 10th layer of the pressure relief panels above the tunnel, and y_1 is the arithmetic mean value of peak pressure of positions #1 and #2 in the experiment (see Fig. 10). y_2 is the arithmetic mean value of the peak impulse of positions #1 and #2 in the experiment. Since positions #1 and #2 were close (0.4 m away from each other), and their pressure history curves were similar in trend and shape, the arithmetic mean of the 2 positions was used to reduce the number of variables and alleviate the difficulty in solving the mathematical model. Hence, y_1=2.76 bar, y_2=37942 Pa·s. As shown in Fig. 10, the pressure period that caused the deformation of concrete slabs is $\triangle P_2$, so the main purpose is to reproduce $\triangle P_2$. The shape of $\triangle P_2$ can be approximately simplified as a triangle. y_1 is the height of the triangle, and y_2 is the area of the triangle. When y_1 and y_2 were determined, the duration of $\triangle P_2$ was determined.

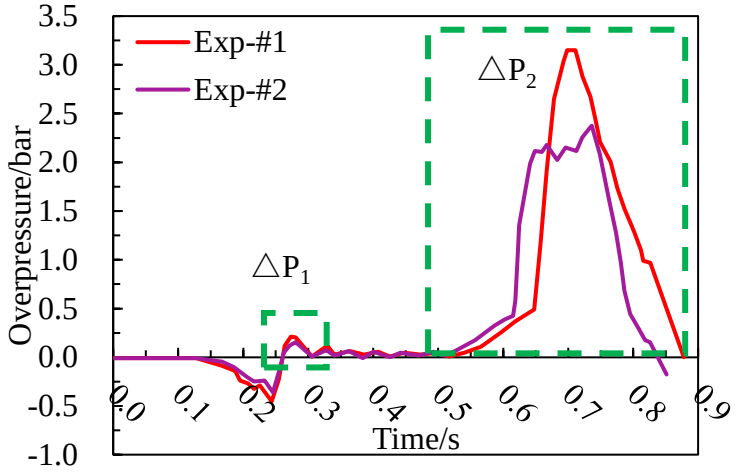

Fig. 10. The overpressure curves at #1 and #2 positions.

The initial values of x_1, x_2 and x_3 were estimated using the typical method for the fixed vented gas explosion and the values were 4.7×10^{-4}, 2.5×10^{-3} and 5.8×10^{-2} bar, respectively. They were going to be adjusted to proper values through the procedure presented in Fig. 10. The values of x_4 to x_{12} were totally blind and no available evidence could be used to assess their values, so they were estimated.

The following procedure was proposed to solve this mathematical model. Even with the assumption that each layer of the pressure relief panels had the same activation pressure, numerous simulations were needed to be tried when every potential solution was tested, as the potential combinations of activation pressures were still large. Here an optimized procedure was proposed to diminish the variables, decrease the numerical simulation time and finally simplify the process. As shown in Fig. 11, correlation analysis was conducted to exclude non-key variables, and ANN was utilized to replace the numerical simulation process to filter the solutions that were inconsistent with the experimental results.

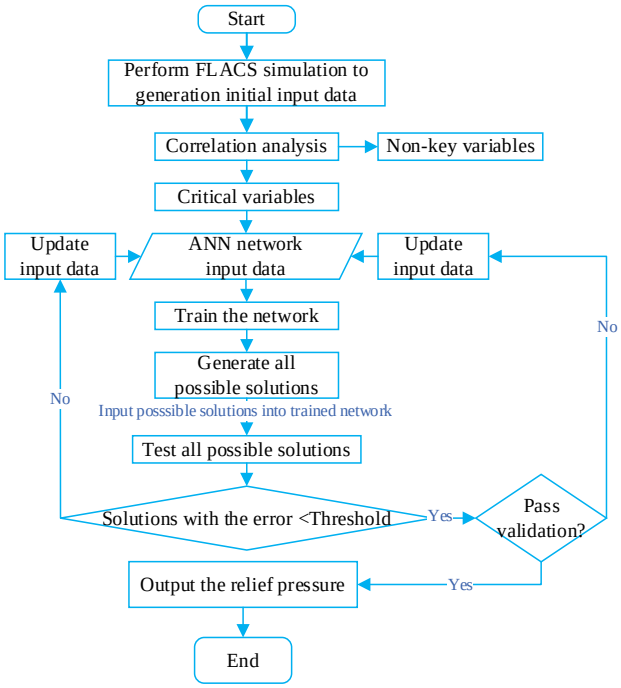

Fig. 11. Flow chart of solving the ANN-numerical hybrid model.

At first, some initial input data were generated. Different values and combinations of x_1 to x_{12} were chosen randomly. Subsequently the corresponding simulation results were obtained through numerical simulation. Based on the numerical results and corresponding x_1 to x_{12}, the correlation coefficient among the activation pressure of the pressure relief panels and peak pressure as well as peak impulse can be calculated. Here, the Pearson correlation coefficient (Fu et al., 2020) was calculated through Eq. (3).

$$r(x,y)=\frac{\sum_{i=1}^{n}\left[(x_i-\bar{x})\cdot(y_i-\bar{y})\right]}{\sqrt{\sum_{i=1}^{n}(x_i-\bar{x})^2}\cdot\sqrt{\sum_{i=1}^{n}(y_i-\bar{y})^2}} \tag{3}$$

where $r(x,y)$ is the correlation coefficient between x and y. The closer the value is to +1 or -1, the stronger the correlation. x represents x_1 to x_{12}. y represents y_1 and y_2. n refers to the sample number of input data. $\bar{x}$ and $\bar{y}$ denote the mean values of the two variables. It is generally known that $0.6\leqslant r(x,y)<0.8$ represents high correlations, and $r(x,y)>0.8$ represents very high correlations. These variables with relatively low correlations were known as non-key variables, which would be excluded from the following numerical model, while those with relatively high correlations were defined as critical variables.

Then, ANN was employed to fit the variables and corresponding results. A typical backpropagation neural network with 1 input layer, 1 hidden layer and 1 output layer was

used. The topology of the BP (backpropagation) neural network is shown in Fig. 12. The detailed theory can be found in the literature (Li et al., 2012), here the critical parameters employed in the present study were illustrated. The fractions of samples employed for training and testing are 90% and 10%, respectively. The number of hidden neurons is 10. The activation functions used in the hidden layer and output layer are tansig(x) and purelin(x), respectively. The network training function is trainlm (Levenberg-Marquardt backpropagation). The backpropagation neural network is implemented by using the machine learning toolbox in MATLAB R2018a. The maximum training epochs, the training goal and the training rate are 5000, 10^{-5} and 10^{-2}, respectively. The code used in the present study was uploaded to GitHub (Chen, 2022).

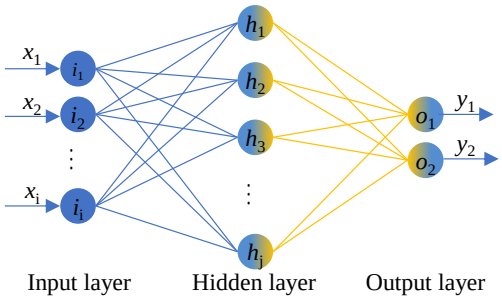

Fig. 12. Structure of the backpropagation neural network.

After the BP neural network finished training, it was employed to yield the outcome of the input data in a much wider range. In this study, 4 level nested loops were utilized to generate all possible combinations of activation pressure of the pressure relief panels. When the error as compared to the experimental results reached a certain threshold, the search stopped and the solutions were output. Of course, this step could be done by numerical simulation, but it would cost much longer time. For example, about 8 hours are needed to finish each single case by performing FLACS at the authors' computer (Intel i9-10900, 5.2 GHz, 32 GB), but only several minutes are needed to test hundreds of solutions with reasonable accuracy when the backpropagation neural network is used. Hence, the neural network is an efficient tool to search for potential solutions in a short time.

Finally, the potential solutions identified by the trained network were validated through FLACS and experimental results. First, FLACS used the corresponding input variables to yield the pressure history curves. Then, these curves were compared with the experimental results to examine whether the numerical results fit with the experimental data. As the numerical results were acceptable, the solving process went to an end. When not, then the numerical results were added to the input data bank of the neural network,

and the network retrained again. As the trained network could not find any satisfying solution, more random numerical solutions were performed to enrich the input data bank.

4.4 Correlation analysis

48 scenarios were simulated. The details of each scenario and numerical results are presented in Table 4. x_1 and x_2 represent the activation pressure of the obstacles inside the tunnel, and it is unreasonable to exclude them from the numerical model as the obstacles have significant impact on load characteristics deriving from gas explosion. Therefore, here only the correlation coefficients among x_3 to x_{12} and y_1, y_2 were calculated.

Table 4. The random numerical simulation results

NO.	x_1 bar	x_2 bar	x_3 bar	x_4 bar	x_5 Bar	x_6 bar	x_7 bar	x_8 bar	x_9 bar	x_{10} bar	x_{11} bar	x_{12} bar	y_1 bar	y_2 Pa • s	Note
1	0.0	0.0	0.00	0.00	0.00	0.00	0.00	0.00	0.00	0.00	0.00	0.00	0.00	12	without obstacles and steel slabs
2	0.0	0.0	5.00	5.00	5.00	5.00	5.00	5.00	5.00	5.00	5.00	5.00	5.31	114842	with steel slabs which had fixed activation pressures and without obstacles
3	6.9×10^{-2}	6.9×10^{-2}	0.00	0.00	0.00	0.00	0.00	0.00	0.00	0.00	0.00	0.00	0.01	13	with obstacles and without steel slabs
4	6.9×10^{-2}	6.9×10^{-2}	5.00	5.00	5.00	5.00	5.00	5.00	5.00	5.00	5.00	5.00	7.76	33459	with obstacles and steel slabs which had fixed activation pressures
5	1.0×10^{-2}	1.0×10^{-2}	1.00	1.00	1.00	1.00	1.00	1.00	1.00	1.00	1.00	1.00	4.12	9754	
6	0.0	6.9×10^{-2}	1.00	1.00	1.00	1.00	1.00	1.00	1.00	1.00	1.00	1.00	3.68	12721	
7	3.3×10^{-3}	1.0×10^{-2}	0.04	1.00	0.88	0.76	0.64	0.52	0.40	0.28	0.16	0.04	1.88	8894	
8	4.7×10^{-4}	2.5×10^{-3}	0.04	2.00	1.76	1.51	1.26	1.02	0.77	0.53	0.28	0.04	2.54	21326	
9	4.7×10^{-4}	2.5×10^{-3}	0.06	3.00	1.00	0.33	0.11	0.04	0.01	0.00	0.00	0.00	3.64	34351	
10	4.7×10^{-4}	2.5×10^{-3}	0.06	4.00	1.33	0.44	0.15	0.05	0.02	0.01	0.00	0.00	4.20	48059	
11	4.7×10^{-4}	2.5×10^{-3}	0.06	5.00	1.67	0.56	0.19	0.06	0.02	0.01	0.00	0.00	5.20	59389	
12	3.3×10^{-3}	1.0×10^{-2}	0.04	0.52	1.00	0.86	0.73	0.59	0.45	0.31	0.18	0.04	1.18	5883	
13	4.7×10^{-4}	2.5×10^{-3}	0.04	1.02	2.00	1.72	1.44	1.16	0.88	0.60	0.32	0.04	1.24	8864	
14	4.7×10^{-4}	2.5×10^{-3}	0.06	1.00	3.00	1.00	0.33	0.11	0.04	0.01	0.00	0.00	1.23	8735	
15	4.7×10^{-4}	2.5×10^{-3}	0.06	1.33	4.00	1.33	0.44	0.15	0.05	0.02	0.01	0.00	1.44	11883	
16	4.7×10^{-4}	2.5×10^{-3}	0.06	1.67	5.00	1.67	0.56	0.19	0.06	0.02	0.01	0.00	2.20	18042	
17	3.3×10^{-3}	1.0×10^{-2}	0.06	0.36	0.68	1.00	0.84	0.68	0.52	0.36	0.20	0.04	0.84	4629	
18	4.7×10^{-4}	2.5×10^{-3}	0.06	0.69	1.35	2.00	1.67	1.35	1.02	0.69	0.37	0.04	1.11	6546	
19	4.7×10^{-4}	2.5×10^{-3}	0.06	0.33	1.00	3.00	1.00	0.33	0.11	0.04	0.01	0.00	0.75	4193	with obstacles and steel slabs which had increasing then decreasing activation pressures
20	4.7×10^{-4}	2.5×10^{-3}	0.06	0.44	1.33	4.00	1.33	0.44	0.15	0.05	0.02	0.01	0.91	4600	
21	4.7×10^{-4}	2.5×10^{-3}	0.06	0.56	1.67	5.00	1.67	0.56	0.19	0.06	0.02	0.01	1.02	5444	
22	3.3×10^{-3}	1.0×10^{-2}	0.06	0.28	0.52	0.76	1.00	0.81	0.62	0.42	0.23	0.04	0.69	4053	
23	4.7×10^{-4}	2.5×10^{-3}	0.06	0.53	1.02	1.51	2.00	1.61	1.22	0.82	0.43	0.04	0.99	4914	
24	4.7×10^{-4}	2.5×10^{-3}	0.06	0.11	0.33	1.00	3.00	1.00	0.33	0.11	0.04	0.01	0.19	2738	
25	4.7×10^{-4}	2.5×10^{-3}	0.06	0.15	0.44	1.33	4.00	1.33	0.44	0.15	0.05	0.02	0.25	3251	
26	4.7×10^{-4}	2.5×10^{-3}	0.06	0.19	0.56	1.67	5.00	1.67	0.56	0.19	0.06	0.02	0.33	3504	
27	3.3×10^{-3}	1.0×10^{-2}	0.06	0.23	0.42	0.62	0.81	1.00	0.76	0.52	0.28	0.04	0.61	3797	
28	4.7×10^{-4}	2.5×10^{-3}	0.06	0.43	0.82	1.22	1.61	2.00	1.51	1.02	0.53	0.04	0.89	4442	
29	4.7×10^{-4}	2.5×10^{-3}	0.06	0.17	0.52	0.75	1.00	3.00	1.00	0.33	0.11	0.04	0.30	3425	
30	4.7×10^{-4}	2.5×10^{-3}	0.06	0.17	0.52	1.57	2.80	4.00	1.33	0.44	0.15	0.05	0.30	3425	
31	4.7×10^{-4}	2.5×10^{-3}	0.06	0.10	0.19	0.56	1.67	5.00	1.67	0.56	0.19	0.06	0.18	2623	
32	3.3×10^{-3}	1.0×10^{-2}	0.06	0.20	0.36	0.52	0.68	0.84	1.00	0.68	0.36	0.04	0.55	3601	

NO.	x_1 bar	x_2 bar	x_3 bar	x_4 bar	x_5 Bar	x_6 bar	x_7 bar	x_8 bar	x_9 bar	x_{10} bar	x_{11} bar	x_{12} bar	y_1 bar	y_2 Pa • s	Note
33	4.7×10^{-4}	2.5×10^{-3}	0.06	0.37	0.69	1.02	1.35	1.67	2.00	1.35	0.69	0.04	0.80	4179	
34	4.7×10^{-4}	2.5×10^{-3}	0.06	0.10	0.18	0.31	0.54	0.95	3.00	1.00	0.33	0.11	0.18	2624	
35	4.7×10^{-4}	2.5×10^{-3}	0.06	0.12	0.23	0.46	0.93	1.86	4.00	1.33	0.44	0.15	0.20	2794	
36	4.7×10^{-4}	2.5×10^{-3}	0.06	0.11	0.22	0.43	0.84	1.64	5.00	1.67	0.56	0.19	0.20	2760	
37	3.3×10^{-3}	1.0×10^{-2}	0.06	0.18	0.31	0.45	0.59	0.73	0.86	1.00	0.52	0.04	0.51	3440	
38	4.7×10^{-4}	2.5×10^{-3}	0.06	0.32	0.60	0.88	1.16	1.44	1.72	2.00	1.02	0.04	0.72	4000	
39	4.7×10^{-4}	2.5×10^{-3}	0.06	0.10	0.17	0.29	0.48	0.82	1.40	3.00	1.00	0.33	0.18	2621	
40	4.7×10^{-4}	2.5×10^{-3}	0.06	0.10	0.18	0.31	0.54	0.95	1.67	4.00	1.33	0.44	0.18	2624	
41	4.7×10^{-4}	2.5×10^{-3}	0.06	0.10	0.18	0.31	0.54	0.95	1.67	5.00	1.67	0.56	0.18	2624	
42	3.3×10^{-3}	1.0×10^{-2}	0.06	0.16	0.28	0.40	0.52	0.64	0.76	0.88	1.00	0.04	0.47	3328	
43	4.7×10^{-4}	2.5×10^{-3}	0.06	0.28	0.53	0.77	1.02	1.27	1.51	1.76	2.00	0.04	0.65	3820	
44	4.7×10^{-4}	2.5×10^{-3}	0.06	0.09	0.15	0.24	0.38	0.61	0.97	1.56	3.00	1.00	0.18	2608	
45	4.7×10^{-4}	2.5×10^{-3}	0.06	0.09	0.15	0.24	0.38	0.61	0.97	1.56	4.00	1.33	0.18	2608	
46	4.7×10^{-4}	2.5×10^{-3}	0.06	0.09	0.15	0.24	0.39	0.64	1.03	1.66	5.00	1.67	0.18	2610	
47	4.7×10^{-4}	2.5×10^{-3}	0.06	2.50	0.83	0.28	0.09	0.03	0.01	0.00	0.00	0.00	2.76	26644	
48	4.7×10^{-4}	2.5×10^{-3}	0.06	3.00	0.00	0.00	0.00	0.00	0.00	0.00	0.00	0.00	3.63	33765	with 2 layers of steel slabs which had fixed activation pressures

The correlation coefficient results are shown in Fig. 13. x_3 and x_4 exhibited the highest correlation with y_1 and y_2 as compared to other layers of activation pressures. It is noticed that x_3 and x_4 are the activation pressure of two layers of the pressure relief panels inside the tunnel.

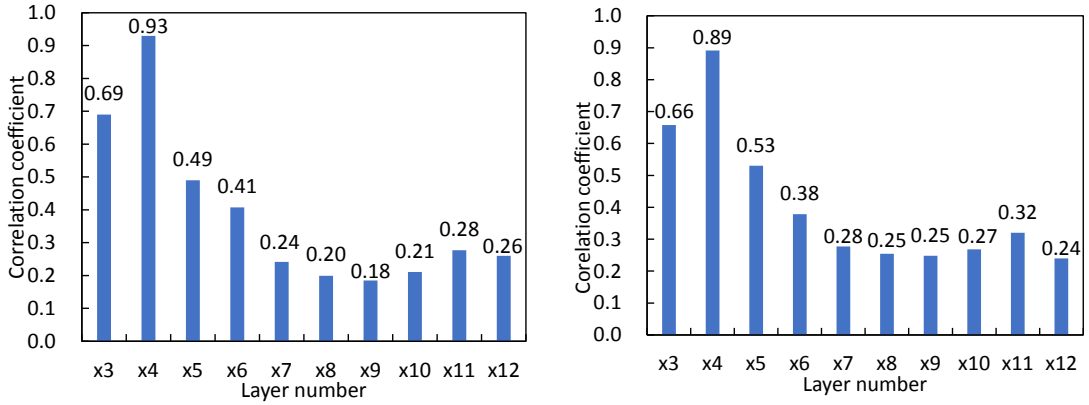

(a) Peak pressure (b) Impulse

Fig. 13. Correlation coefficients between peak pressure/impulse and activation pressure of each layer.

Fig. 14 presents a comparison of the numerical results at 2, 3 and 10 layers of the pressure relief panels above the tunnel. The pressure history curves were quite similar in shape, and the peak impulse with 2 layers was slightly lower than that of 10 layers. Thus, in the following analysis, x_5 to x_{12} were excluded from the numerical model to simplify the solving process. The correlation analysis results revealed that the steel slabs had insignificant impact on the progressive vented gas explosion load after being lifted above the tunnel top.

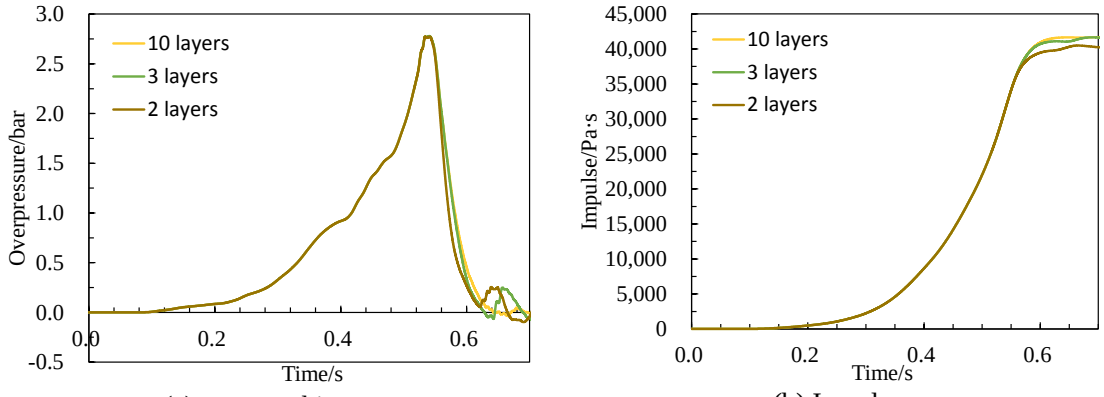

(a) pressure history (b) Impulse

Fig. 14. Result comparison between 2,3 and 10 layers of pressure relief panels.

From the random simulation it follows that the assumption of each layer of the pressure relief panels having the same activation pressure is unreasonable. As shown in Fig. 15, the numerical results indicated that the first venting position was not at the ignition end. But in the experiment, the steel slabs were blown upwards one by one from the ignition

end to the concrete specimen end. The reason for this is that in the actual scenario, the steel slab at the ignition side had the slightest drag force since only one side of the slab was connected with its neighboring slab. By comparison, two sides were connected for these steel slabs that were not placed at the two ends of the tunnel, and an additional frictional force was provided by the concrete specimen for the steel slab adjacent to the concrete. However, for numerical simulation, the activation pressure for the 2nd layer pressure panel was the same, and the panel was opened at the position where the peak pressure reached the predetermined activation pressure. To assess this progressive opening procedure correctly, in the subsequent simulations, the activation pressures of the panels were considered as lower at the ignition end and higher at the other end.

(a) Experimental venting position

(b) Numerical venting position

Fig. 15. Comparison between the experimental and numerical vented positions in the condition that the 2nd layer of pressure relief panels has the same activation pressure.

The correlation analysis and simulation results revealed that x_5 to x_{12} could be excluded from the subsequent numerical model, and the activation pressures for the 2nd layer of pressure relief panels should increase for the panel from the ignition end to the other end of the tunnel. Here, a linear ascent trend was assumed. The numerical model was simplified as shown in Fig. 16 and the mathematical model of Eq. (1) was simplified to:

$$f(x_1, x_2, x_3, x_{4,1}, x_{4,44})=(y_1, y_2) \quad (4)$$

where $x_{4,1}$ represents the activation pressure of the pressure relief panel close to the ignition end, and $x_{4,44}$ represents the activation pressure of the pressure relief panel close to the concrete specimen.

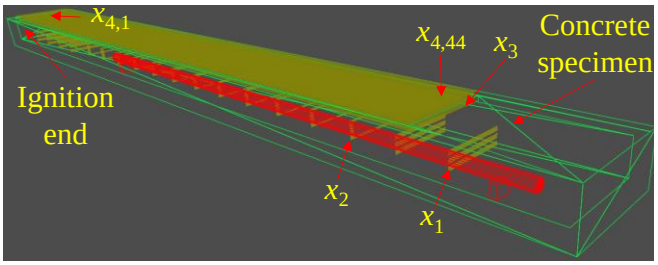

Fig. 16. The simplified numerical model

4.5 ANN-based prediction results

4.5.1 Obstacles with calculated activation pressures

At first, there was no idea to what extent the obstacles could still affect the flow field upon being pushed away from their initial position. Therefore, no further effect upon the

obstacles being moved was assumed, but the activation pressure of obstacles would be close to the pressure at the inception of their moving. A ±15% uncertainty of the friction coefficient was considered, then the values of 4.0×10^{-4}, 4.7×10^{-4} and 5.5×10^{-4} were applied to x_1, and 2.1×10^{-3}, 2.5×10^{-3} and 2.9×10^{-3} were applied to x_2. x_3 exhibited less uncertainty, hence, its value was considered as a constant (0.058 bar).

x_4 demonstrated the highest correlation with y_1, so the values close to y_1 (2.37) were denser with a small gradient, here 2.0, 2.45, 2.9, 4.5, 6.1 were applied to $x_{4,1}$. The random simulation results revealed that the highest overpressure in the tunnel was slightly higher (+0.3 bar or so) than the activation pressure of the steel slabs. To simulate the progressive failure process, each $x_{4,1}$ plus 0.1, 0.3, 0.5 was applied to $x_{4,44}$. For example, when $x_{4,1}$ was 2.0, $x_{4,44}$ was 2.1, 2.3, 2.5, respectively. The range of x_1, x_2, x_3, $x_{4,1}$, $x_{4,44}$ is presented in Table 5, and the corresponding values were applied in the numerical model to generate ANN input data.

Table 5 The range of x_1, x_2, x_3, $x_{4,1}$, $x_{4,44}$ (bar)

x_1	x_2	x_3	$x_{4,1}$	$x_{4,44}$
4.0×10^{-4}	2.1×10^{-3}		2.0	
4.7×10^{-4}	2.5×10^{-3}		2.45	
5.5×10^{-4}	2.9×10^{-3}	0.058	2.9	$x_{4,1}$+0.1, 0.3, 0.5
-	-		4.5	
-	-		6.1	

The simulation results are presented in Table 6, and the training and simulation results are illustrated in Fig. 17. A comparison between the numerical and ANN results indicates that the ANN-based tool has a good capability to fit the numerical data.

Table 6 The ANN input data

NO.	x_1 bar	x_2 bar	x_3 Bar	$x_{4,1}$ bar	$x_{1,44}$ bar	y_1 bar	y_2 Pa • s
1	4.7×10^{-4}	2.5×10^{-3}	0.058	4.50	4.60	4.72	68739
2	4.7×10^{-4}	2.5×10^{-3}	0.058	4.50	4.80	4.82	74290
3	4.7×10^{-4}	2.5×10^{-3}	0.058	4.50	5.00	4.84	77543
4	5.5×10^{-4}	2.1×10^{-3}	0.058	6.10	6.20	6.31	127846
5	5.5×10^{-4}	2.1×10^{-3}	0.058	6.10	6.40	6.34	130882
6	5.5×10^{-4}	2.1×10^{-3}	0.058	6.10	6.60	6.36	131975
7	4.0×10^{-4}	2.9×10^{-3}	0.058	2.00	2.10	2.26	31037
8	4.7×10^{-4}	2.5×10^{-3}	0.058	2.45	2.75	3.14	42337
9	4.7×10^{-4}	2.5×10^{-3}	0.058	2.45	2.95	3.24	43655
10	5.5×10^{-4}	2.1×10^{-3}	0.058	2.90	3.00	3.09	46685
11	5.5×10^{-4}	2.1×10^{-3}	0.058	2.90	3.20	3.30	49752
12	5.5×10^{-4}	2.1×10^{-3}	0.058	2.90	3.40	3.44	53320
13	4.7×10^{-4}	2.9×10^{-3}	0.058	6.10	6.20	6.09	128829
14	4.7×10^{-4}	2.9×10^{-3}	0.058	6.10	6.40	6.24	135113
15	4.7×10^{-4}	2.9×10^{-3}	0.058	6.10	6.60	6.24	137380

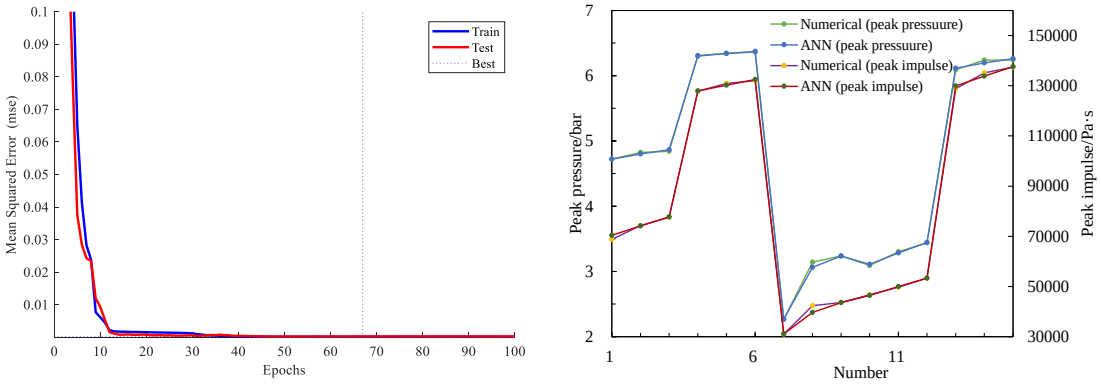

(a) The convergence curve (b) Comparison between numerical and ANN results

Fig. 17 ANN training result

In view of the trained network, a possible solution of x_1=4.5 × 10^{-4}, x_2=2.6 × 10^{-3}, x_3=0.058, $x_{4,1}$=2.0, $x_{4,44}$=2.3, $y_{1,ANN}$=2.76 and $y_{2,ANN}$=38079 was observed within the range of $x_1 \in (4.0 \times 10^{-4}, 6.0 \times 10^{-4})$, $x_2 \in (2.0 \times 10^{-3}, 3.0 \times 10^{-3})$, x_3=0.058, $x_{4,1} \in (1, 4)$ and $x_{4,44} \in (1.1, 4.5)$, and a total of 3×10^4 combinations were tested by the ANN network. Subsequently, this solution was tested through the numerical simulation. A comparison of ANN and numerical results are presented in Table 7. The deviation between the ANN and numerical results indicated the trained BP network had a good ability to predict the numerical results.

Table 7 The comparison of ANN and numerical results

Parameter	ANN	Numerical	error
y_1	2.76	2.56	7.9%
y_2	38079	36212	5.2%

A comparison of the numerical results with experimental data is depicted in Fig. 18. The peak pressure of △P2 predicted by the numerical model was observed to coincide with the experimental findings well, and the predicted peak impulse was close to the experimental data. However, the rate of pressure rise of the simulation result was slower as compared to the experimental findings.

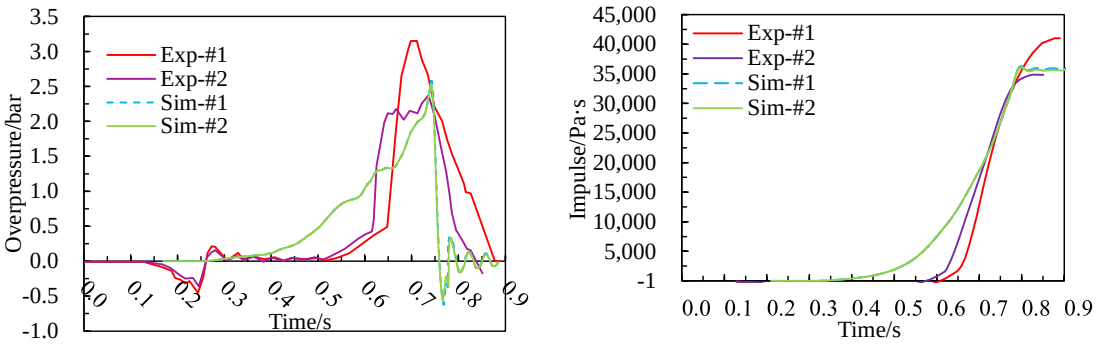

(a) Pressure history curve (b) Impulse curve

Fig. 18 The comparison between the numerical and experimental results

No further influence upon the obstacles being moved was assumed in this section, but the numerical model produced a lower rate of pressure rise which would lead to different structural responses (Caçoilo et al., 2021). In the experimental scenario, the obstacles still stayed in the tunnel for a while, which had an impact on the flow field upon being pushed away from their initial positions. Therefore, obstacles with larger activation pressures than calculated ones were studied to reveal to what extent these obstacles influenced the flow field upon being moved.

4.5.2 Obstacles with larger activation pressures than the calculated ones

The activation pressure of obstacles was increased to emulate their effect on the flow field after being moved, so x_1, x_2 were increased to as much as 5 times as their calculation values. The range of x_1, x_2, x_3, $x_{4,1}$, $x_{4,44}$ is presented in Table 8, and the corresponding values were applied to the numerical model to generate ANN input data.

Table 8 The range of x_1, x_2, x_3, $x_{4,1}$, $x_{4,44}$ (bar)

x_1	x_2	x_3	$x_{4,1}$	$x_{4,44}$
4.7×10^{-3}	2.5×10^{-3}		1.7	
1.4×10^{-3}	7.5×10^{-3}		2.0	
2.4×10^{-3}	1.3×10^{-2}	0.058	2.3	$x_{4,1}$+0.1, 0.3, 0.5
-	-		2.6	
-	-		2.9	

The simulation results are presented in Table 9, and the training and simulation findings are displayed in Fig. 19.

Table 9 The ANN input data

NO.	x_1 bar	x_2 bar	x_3 bar	$x_{4,1}$ bar	$x_{1,44}$ bar	y_1 bar	y_2 Pa • s
1	4.7×10^{-3}	2.5×10^{-3}	0.058	1.70	1.80	1.88	29353
2	4.7×10^{-3}	2.5×10^{-3}	0.058	1.70	2.00	2.08	32274
3	4.7×10^{-3}	2.5×10^{-3}	0.058	1.70	2.30	2.18	37409
4	2.4×10^{-3}	1.3×10^{-2}	0.058	2.30	2.40	3.24	19452
5	2.4×10^{-3}	1.3×10^{-2}	0.058	2.30	2.60	3.52	20230
6	2.4×10^{-3}	1.3×10^{-2}	0.058	2.30	2.80	3.89	21667
7	1.4×10^{-3}	2.5×10^{-3}	0.058	2.90	3.00	3.14	45541
8	1.4×10^{-3}	2.5×10^{-3}	0.058	2.90	3.20	3.41	48223
9	1.4×10^{-3}	2.5×10^{-3}	0.058	2.90	3.40	3.47	54950
10	1.4×10^{-3}	7.5×10^{-3}	0.058	2.00	2.1	2.49	19735
11	1.4×10^{-3}	7.5×10^{-3}	0.058	2.00	2.3	2.69	20675
12	1.4×10^{-3}	7.5×10^{-3}	0.058	2.00	2.5	2.94	21888
13	1.4×10^{-3}	1.3×10^{-2}	0.058	2.60	2.70	3.12	24220
14	1.4×10^{-3}	1.3×10^{-2}	0.058	2.60	2.90	3.43	25865
15	1.4×10^{-3}	1.3×10^{-2}	0.058	2.60	3.10	3.62	26926

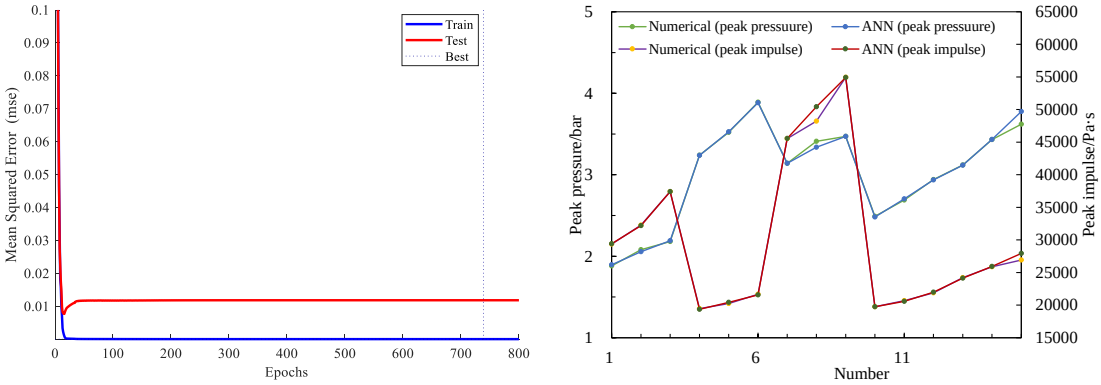

(a) The convergence curve (b) Comparison between numerical and ANN results

Fig. 19 ANN training results

Based on the trained network, a possible solution of x_1=1.2×10^{-3}, x_2=6.3×10^{-3}, x_3=0.058, $x_{4,1}$=2.30, $x_{4,44}$=2.85, $y_{1,\mathrm{ANN}}$=2.77 and $y_{2,\mathrm{ANN}}$=37934 was achieved within the range of x_1 ∈(4.7×10^{-4}, 2.4×10^{-3}), x_2∈(2.5×10^{-3}, 1.3×10^{-2}), x_3=0.058, $x_{4,1}$∈(1, 4) and $x_{4,44}$∈(1.1, 4.5), and a total of 66×10^4 combinations were tested by the ANN network. Afterwards, the solution was tested by the numerical model. The comparison of the ANN and numerical results is shown in Table 10.

Table 10 The comparison of ANN and numerical results

Parameter	ANN	Numerical	error
y_1	2.77	2.758	0.05%
y_2	37934	45137	-16.0%

The comparison between the numerical and experimental results is presented in Fig. 20 and Table 11. The history curves predicted by FLACS agreed well with the experimental ones. As seen in Fig. 21, the flame development from the tunnel gas vented explosion was projected in FLACS 3D view. In this simulation, the falling process of the steel slabs was not modeled. The determined x_1 and x_2 were 2.56 and 2.51 times as large as their calculated values, respectively, indicating their contribution to the flow field could not be ignored upon being pushed away from initial positions.

FLACS did not replicate the first overpressure peak of $\triangle P_1$ generated by the combination of gas combustion and gas escape from small gaps (Yang et al., 2021). These gaps were only several millimeters, whereas the numerical model was unable to mimic them since the grid resolution of 2 cm or less in explosion simulations is not recommended (Gexcon, 2019).

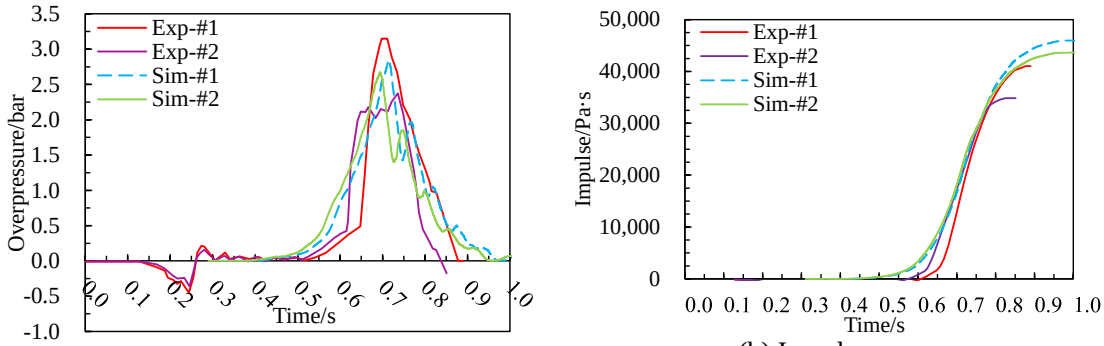

(a) Pressure history curve (b) Impulse curve

Fig. 20 The comparison between the numerical and experimental results

Table 11 The comparison of experimental and numerical results

Parameter	Experimental		Numerical	
	#1	#2	#1	#2
Peak pressure (bar)	3.15	2.37	2.84	2.67
Error	/	/	-9.8%	12.7%
Peak impulse (Pa·s)	41039	34868	46316	43959
Error	/	/	12.9%	26.1%

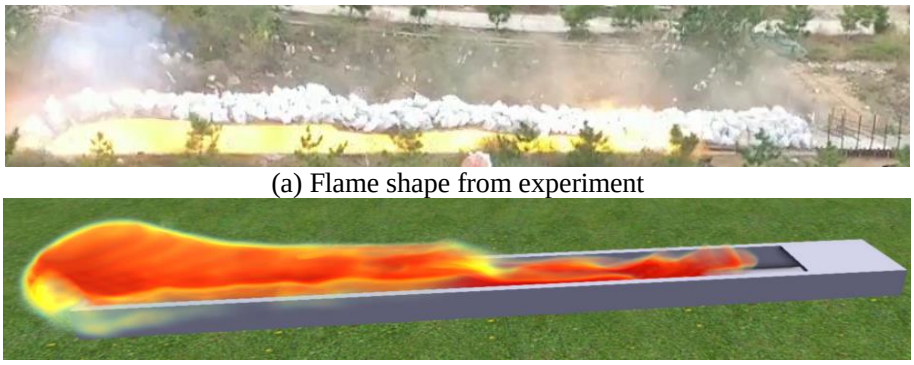

(a) Flame shape from experiment

(b) Flame shape from simulation

Fig. 21 Flame shape comparison

5 Conclusions

The modelling of a progressive vented gas explosion was presented using a CFD tool. Fixed vented gas explosion tests were used to validate the numerical model. The experimental results of a large-scale progressive vented gas explosion in a utility tunnel were utilized for further validation. A modified method based on a combination of the mathematical model and artificial neural network (ANN) was employed to help determine the critical parameters of the proposed model.

Generally, the numerical data matched with the experimental results. For the fixed vented gas explosion scenarios, the multiple overpressure peaks were predicted within satisfying error range by applying the first pressure peak as the activation pressure of the pressure relief panels, and the pressure history curves were roughly consistent with experimental

data. For the progressive vented gas explosion scenario, it was more challenging to replicate the experimental results owing to its complex boundary conditions. The method which was suitable for fixed vented gas explosion to estimate the activation pressure of the pressure relief panels underestimated the overpressure for the progressive vented gas explosion. According to the correlation analysis among the activation pressure of the pressure relief panels and peak pressure as well as peak impulse, the vent covers had an insignificant impact on the gas explosion load after being lifted over the tunnel top. The falling process of the vent covers was not necessary to be modelled. The progressive vented gas explosion process could be modelled by two-layer pressure relief panels with the activation pressures of the upper layer having a linear ascent trend from the ignition end to the other end. The activation pressures of obstacles inside the tunnel were about 2.5 times as large as their calculated value, indicating the obstacles' contribution to the flow field could not be ignored upon being pushed away from initial positions. An ANN-based tool was utilized to help determine the critical parameters in the numerical model, so as to save computational time involved in pure numerical simulation.

Acknowledgements

This work was supported by the Australia Research Council under ARC Discovery Project DP210101100.

References

Arntzen, B.J., 1998. Modelling of turbulence and combustion for simulation of gas explosions in complex geometries. Dr. Ing. Thesis., https://ntnuopen.ntnu.no/ntnu-xmlui/bitstream/handle/11250/227921/122240_FULLTEXT01.pdf?sequence=1&isAllowed=y.

Bakke, J.R., Skogrand, P.E., Asa, A.K., 2004. Explosion Relief Panels and Their Effect on Gas Explosion Overpressure. 1-8, http://doi.org/10.1115/OMAE2004-51005.

Bleyer, A., Taveau, J., Djebaïli-Chaumeix, N., Paillard, C.E., Bentaïb, A., 2012. Comparison between FLACS explosion simulations and experiments conducted in a PWR Steam Generator casemate scale down with hydrogen gradients. Nucl. Eng. Des. 245, 189-196, http://doi.org/10.1016/j.nucengdes.2012.01.010.

BP, P.L.C., 2021. Statistical Review of World Energy. https://www.bp.com/content/dam/bp/business-sites/en/global/corporate/pdfs/energy-economics/statistical-review/bp-stats-review-2021-full-report.pdf.

Caçoilo, A., Mourão, R., Teixeira-Dias, F., Lecompte, D., Rush, D., 2021. Structural response of corrugated plates under blast loading: The influence of the pressure-time history. Structures 30, 531-545, http://doi.org/10.1016/j.istruc.2021.01.025.

Cheng, L., Li, S., Ma, L., Li, M., Ma, X., 2015. Fire spread simulation using GIS: Aiming at urban natural gas pipeline. Safety Sci. 75, 23-35, http://doi.org/10.1016/j.ssci.2015.01.002.

Chmielewski, R., Bąk, A., 2021. Analysis of the safety of residential buildings under gas explosion loads. Journal of Building Engineering 43, 102815, http://doi.org/10.1016/j.jobe.2021.102815.

Cooper, M.G., Fairweather, M., Tite, J.P., 1986. On the Mechanisms of Pressure Generation in Vented Explosions. Combust. Flame 1, 1-14, http://doi.org/10.1016/0010-2180(86)90067-2.

Department Of Defense, 2008. Structures To Resist The Effects Of Accidental Explosions. https://www.wbdg.org/ffc/dod/unified-facilities-criteria-ufc/ufc-3-340-02

Pressure relief panel failure pressure prediction, 2022. https://github.com/DearChen6666/pressure-relief-panel-failure-pressure-prediction

European Committee for Standardization., 2007. Gas explosion venting protective systems. https://cdn.standards.iteh.ai/samples/14897/d43645766c484520bca5b8ea2f9436b0/SIST-EN-14994-2007.pdf

Fu, T., Tang, X., Cai, Z., Zuo, Y., Tang, Y., Zhao, X., 2020. Correlation research of phase angle variation and coating performance by means of Pearson's correlation coefficient. Prog. Org. Coat. 139, 105459, http://doi.org/10.1016/j.porgcoat.2019.105459.

Gexcon, 2019. FLACS v10.9 User's Manual.

Guo, J., Wang, C., Li, Q., Chen, D., 2016. Effect of the vent burst pressure on explosion venting of rich methane-air mixtures in a cylindrical vessel. J. Loss Prevent. Proc. 40, 82-88, http://doi.org/10.1016/j.jlp.2015.12.006.

Jaaranen, J., Fink, G., 2020. Frictional behaviour of timber-concrete contact pairs. Constr. Build. Mater. 243, 118273, http://doi.org/10.1016/j.conbuildmat.2020.118273.

Kasmani, R.M., Andrews, G.E., Phylaktou, H.N., 2013. Experimental study on vented gas explosion in a cylindrical vessel with a vent duct. Process Saf. Environ. 91, 245-252, http://doi.org/10.1016/j.psep.2012.05.006.

Kumar, A., 1994. Guidelines for Evaluating the Characteristics of Vapor Cloud Explosions, Flash Fires, and BLEVEs, American Institute of Chemical Engineers, New York, USA.

Launder, B.E., Spalding, D.B., 1974. The numerical computation of turbulent flows. Comput. Method. Appl. M. 3, 269–289, http://doi.org/10.1016/b978-0-08-030937-8.50016-7.

Li, F.G., Chen, L., 2014. Gas Explosion Effect on Structure Damage and Control Measures. Applied Mechanics and Materials 501-504, 2424-2427, http://doi.org/10.4028/www.scientific.net/AMM.501-504.2424.

Li, J., Cheng, J., Shi, J., Huang, F., 2012.Brief Introduction of Back Propagation (BP) Neural Network Algorithm and Its Improvement, in:(Eds.), Springer Berlin Heidelberg, Berlin, Heidelberg, pp. 553-558.

Li, J., Hao, H., 2018. Far-field pressure prediction of a vented gas explosion from storage tanks by using new CFD simulation guidance. Process Saf. Environ. 119, 360-378, http://doi.org/10.1016/j.psep.2018.08.004.

Li, J., Hao, H., 2019. Numerical and analytical prediction of pressure and impulse from vented gas explosion in large cylindrical tanks. Process Saf. Environ. 127, 226-244, http://doi.org/10.1016/j.psep.2019.05.019.

Li, J., Hernandez, F., Hao, H., Fang, Q., Xiang, H., Li, Z., Zhang, X., Chen, L., 2017. Vented Methane-air Explosion Overpressure Calculation—A simplified approach based on CFD. Process Saf. Environ. 109, 489-508, http://doi.org/10.1016/j.psep.2017.04.025.

[a]Li, Z., Chen, L., Fang, Q., Chen, W., Hao, H., Zhang, Y., 2017. Experimental and numerical study of basalt fiber reinforced polymer strip strengthened autoclaved aerated concrete masonry walls under vented gas explosions. Eng. Struct. 152, 901-919, http://doi.org/10.1016/j.engstruct.2017.09.055.

[b]Li, Z., Chen, L., Fang, Q., Chen, W., Hao, H., Zhu, R., Zheng, K., 2019. Experimental and numerical study on CFRP strip strengthened clay brick masonry walls subjected to vented gas explosions. Int. J. Impact Eng. 129, 66-79, http://doi.org/10.1016/j.ijimpeng.2019.02.013.

[c]Li, Z., Chen, L., Fang, Q., Hao, H., Zhang, Y., Chen, W., Xiang, H., Bao, Q., 2017. Study of autoclaved aerated concrete masonry walls under vented gas explosions. Eng. Struct. 141, 444-460, http://doi.org/10.1016/j.engstruct.2017.03.033.

[d]Li, Z., Chen, L., Fang, Q., Hao, H., Zhang, Y., Xiang, H., Chen, W., Yang, S., Bao, Q., 2017. Experimental and numerical study of unreinforced clay brick masonry walls subjected to vented gas explosions. Int. J. Impact Eng. 104, 107-126, http://doi.org/10.1016/j.ijimpeng.2017.02.002.

Lucas, M., Atanga, G., Hisken, H., Mauri, L., Skjold, T., 2021. Simulating vented hydrogen deflagrations: Improved modelling in the CFD tool FLACS-hydrogen. Int. J. Hydrogen Energ. 46, 12464-12473, http://doi.org/10.1016/j.ijhydene.2020.09.073.

Meng, Q., Wu, C., Hao, H., Li, J., Wu, P., Yang, Y., Wang, Z., 2020. Steel fibre reinforced alkali-activated geopolymer concrete slabs subjected to natural gas

explosion in buried utility tunnel. Constr. Build. Mater. 246, 118447, http://doi.org/10.1016/j.conbuildmat.2020.118447.

[a]Meng, Q., Wu, C., Li, J., Liu, Z., Wu, P., Yang, Y., Wang, Z., 2020. Steel/basalt rebar reinforced Ultra-High Performance Concrete components against methane-air explosion loads. Composites Part B: Engineering 198, 108215, http://doi.org/10.1016/j.compositesb.2020.108215.

[b]Meng, Q., Wu, C., Li, J., Liu, Z., Wu, P., Yang, Y., Wang, Z., 2020. Steel/basalt rebar reinforced Ultra-High Performance Concrete components against methane-air explosion loads. Composites Part B: Engineering 198, 108215, http://doi.org/10.1016/j.compositesb.2020.108215.

Meng, Q., Wu, C., Li, J., Wu, P., Xu, S., Wang, Z., 2021. A study of pressure characteristics of methane explosion in a 20 m buried tunnel and influence on structural behaviour of concrete elements. Eng. Fail. Anal. 122, 105273, http://doi.org/10.1016/j.engfailanal.2021.105273.

National Fire Protection Association, 2007. Standard on Explosion Protection by Deflagration Venting. https://www.nfpa.org/codes-and-standards/all-codes-and-standards/list-of-codes-and-standards/detail?code=68

Nishimura, I., Mogi, T., Dobashi, R., 2013. Simple method for predicting pressure behavior during gas explosions in confined spaces considering flame instabilities. J. Loss Prevent. Proc. 26, 351-354, http://doi.org/10.1016/j.jlp.2011.08.009.

Park, D.J., Lee, Y.S., Green, A.R., 2008. Experiments on the effects of multiple obstacles in vented explosion chambers. J. Hazard. Mater. 153, 340-350, http://doi.org/10.1016/j.jhazmat.2007.08.055.

Pedersen, H.H., Middha, P., 2012. Modelling of Vented Gas Explosions in the CFD tool FLACS. Chemical engineering transactions 26, http://doi.org/10.3303/CET1226060.

Pedersen, H.H., Tomlin, G., Middha, P., Phylaktou, H.N., Andrews, G.E., 2013. Modelling large-scale vented gas explosions in a twin-compartment enclosure. J. Loss Prevent. Proc. 26, 1604-1615, http://doi.org/10.1016/j.jlp.2013.08.001.

Rabbat, B.G., Asce, M., Russell, H.G., 1985. Friction Coefficient of Steel on Concrete or Grout. J. Struct. Eng. 111, 505-515, http://doi.org/10.1061/(ASCE)0733-9445(1985)111:3(505).

Salaun, N., Arve, G.H., Per, E.N., 2016. Risk-based Structural Response against Explosion Blast Loads: Systematic One-to-one CFD (FLACS) / NLFEA (Impetus Afea solver) Coupling to Derive Quantified Response Exceedance. Chemical engineering transactions 48, http://doi.org/10.3303/CET1648010.

Tolias, I.C., Giannissi, S.G., Venetsanos, A.G., Keenan, J., Shentsov, V., Makarov, D., Coldrick, S., Kotchourko, A., Ren, K., Jedicke, O., Melideo, D., Baraldi, D., Slater, S., Duclos, A., Verbecke, F., Molkov, V., 2019. Best practice guidelines in

numerical simulations and CFD benchmarking for hydrogen safety applications. Int. J. Hydrogen Energ. 44, 9050-9062, http://doi.org/10.1016/j.ijhydene.2018.06.005.

Tomlin, G., Johnson, D.M., Cronin, P., Phylaktou, H.N., Andrews, G.E., 2015. The effect of vent size and congestion in large-scale vented natural gas/air explosions. J. Loss Prevent. Proc. 35, 169-181, http://doi.org/10.1016/j.jlp.2015.04.014.

Vyazmina, E., Jallais, S., 2016. Validation and recommendations for FLACS CFD and engineering approaches to model hydrogen vented explosions: Effects of concentration, obstruction vent area and ignition position. Int. J. Hydrogen Energ. 41, 15101-15109, http://doi.org/10.1016/j.ijhydene.2016.05.189.

Wang, Q., Luo, X., Wang, C., Liu, Y., Zhou, P., Li, B., 2022. Experimental study on external explosion for vented hydrogen deflagration in a rectangular tube with different vent coefficients. Process Saf. Environ. 158, 331-339, http://doi.org/10.1016/j.psep.2021.12.002.

Xing, H., Xu, Q., Song, X., Wang, Y., Li, B., Xie, L., 2020. The effects of vent area and ignition position on pressure oscillations in a large L/D ratio duct. Process Saf. Environ. 135, 166-170, http://doi.org/10.1016/j.psep.2019.12.030.

Yang, H., Chen, J., Chiu, H., Kao, T., Tsai, H., Chen, J., 2016. Confined vapor explosion in Kaohsiung City – A detailed analysis of the tragedy in the harbor city. J. Loss Prevent. Proc. 41, 107-120, http://doi.org/10.1016/j.jlp.2016.03.017.

Yang, Y., Wu, C., Liu, Z., Du, J., Zhang, H., Xu, S., Zhou, S., 2021. Protective effect of unbonded prestressed ultra-high performance reinforced concrete slab against gas explosion in buried utility tunnel. Process Saf. Environ. 149, 370-384, http://doi.org/10.1016/j.psep.2020.11.002.

Yu, M., Wan, S., Zheng, K., Guo, P., Chu, T., Yuan, Z., 2017. Influence on the methane/air explosion characteristics of the side venting position in a pipeline. Process Saf. Environ. 111, 292-299, http://doi.org/10.1016/j.psep.2017.07.017.

Zhu, Y., Qian, X., Liu, Z., Huang, P., Yuan, M., 2015. Analysis and assessment of the Qingdao crude oil vapor explosion accident: Lessons learnt. J. Loss Prevent. Proc. 33, 289-303, http://doi.org/10.1016/j.jlp.2015.01.004.

Zhu, Y., Wang, D., Shao, Z., Zhu, X., Xu, C., Zhang, Y., 2020. Investigation on the overpressure of methane-air mixture gas explosions in straight large-scale tunnels. Process Saf. Environ. 135, 101-112, http://doi.org/10.1016/j.psep.2019.12.022.

A numerical study of gas explosion with progressive venting in a utility tunnel

Di Chen[a, b], Chengqing Wu[a], Jun Li[a], Kexi Liao[b]

[a] *School of Civil and Environmental Engineering, University of Technology Sydney, Sydney, NSW, 2007, Australia*

[b] *School of Oil & Natural Gas Engineering, Southwest Petroleum University, Chengdu, Sichuan, 610500, China*

Keywords: CFD; gas explosion; progressive venting; moving obstacle; artificial neural network

Abstract

A numerical model of a progressive vented gas explosion is presented. A CFD tool in combination with correlation analysis and an artificial neural network (ANN) were utilized to establish and refine the numerical model. The experimental results of 44 fixed vented gas explosions and one progressive vented gas explosion with moving obstacles were used to validate the numerical accuracy. The results indicated that the method to estimate the activation pressure of the pressure relief panels for a fixed vented gas explosion achieved a lower overpressure prediction compared to that for a progressive vented gas explosion. The progressive venting procedure was modelled by two-layer pressure relief panels with the upper layer having activation pressures with a linear ascent trend. The vents on the tunnel had an insignificant impact on the explosion load after being lifted over the tunnel top, and their falling process was unnecessary to be modelled. A non-negligible impact of the obstacles inside the tunnel on the flow field upon being pushed away from their initial positions was demonstrated. By employing an ANN, the critical parameters in the numerical model were determined, which were used to accurately replicate the experimental results. The findings clarified a revenue for the modeling of a progressive vented gas explosion as well as some shortcomings of the CFD tool.

1 Introduction

Natural gas is a widely used energy source in daily life and industrial production. In 2020, natural gas contributed 24.7% of the total energy consumption globally, reaching a record high even though the pandemic reduced energy consumption (BP 2021). With ever-increasing popularity, safety issues in the natural gas transportation, storage and end-use

are attracting increasingly more attention. In fact, natural gas explosion accidents are not uncommon in the world and may cause enormous casualties and economic losses (Cheng et al., 2015).

Venting of a gas explosion represents an effective way to mitigate the blast effects on human beings and structures (Chmielewski and Bąk, 2021; Li and Chen, 2014). Carefully designed venting devices ensure the reduction in blast pressure. For example, the maximum overpressure of approximately 2.2 bars was observed in a series of natural gas explosion tests conducted in a 4.5m×4.5m×9m container with vent openings (Tomlin et al., 2015). By comparison, the maximum pressure of 7.8 bars was captured in a totally confined 0.12 m^3 spherical container (Nishimura et al., 2013).

Vented gas explosions have been studied experimentally and numerically. An experiment is the most direct and reliable way to investigate governing factors affecting the vented gas explosion characteristics. Cooper et al. (Cooper et al., 1986) performed a series of gas explosion tests in near-cubic enclosures with pressure relief panels, and 4 evident pressure peaks were identified. As shown in Fig. 1, P_1 was generated prior to the opening of the relief panel which was attributed to the gas expansion in a confined reaction vessel owing to combustion. After the relief panel was broken, a certain amount of unburned methane-air mixture was expelled from the container and continued combusting outside the vessel, which resulted in a sharp increment in the internal pressure known as P_2. P_3 occurred when the flame occupied the largest space in the vessel. The peak pressure P_4 was generated by the coupling of the combustion process with acoustic modes of the vessel. It was reported that the acoustically enhanced P_4 would not be of importance in a wide range of practical situations. Park et al. (Park et al., 2008) examined the flame interaction with different obstacle arrangements and pointed out that a higher overpressure would be induced by stronger turbulence caused by obstacles. Kasmani et al. (Kasmani et al., 2013) conducted a series of gas explosion tests in a cylindrical vessel connected with a vent duct to explore the influence of vent burst pressure and ignition location on overpressures, and concluded that the vent burst pressure was complex and a non-linear effect was observed which did not coincide with the design standard of NFPA 68 (National Fire Protection Association, 2007). Tomlin et al. (Tomlin et al., 2015) conducted 38 vented gas explosion tests in a 182 m^3 explosion chamber with different vent and congestion situations, indicating that a damaging overpressure could be derived even in empty enclosures as the venting size was insufficient and the presence of obstacles enhanced the overpressure significantly. Guo et al. (Guo et al., 2016) studied the effect of the activation pressure of vent panels on the explosion load in a cylindrical vessel, and demonstrated that the maximum overpressure increased approximately linear with the activation pressure of vent panels. Li et al. (Li and Hao, 2018, 2019; Li et al., 2017) conducted a series of in-

situ tests in large-scale storage tanks to explore the effect of the enclosure scale, vent condition and gas concentration on the pressure load characteristics. Li et al. ([a]Li et al., 2017; [b]Li et al., 2019; [c]Li et al., 2017; [d]Li et al., 2017) investigated the effect of gas concentration and vent opening characteristics both on load characteristics and structural response through full-scale in-situ tests, and concluded that the design guides (NFPA68 (Association, 2007) and EN 14994 (European Committee for Standardization, 2007)) and the TNT-equivalency method suggested by CCPS (Kumar, 1994) as well as UFC3-340-02 (Department Of Defense, 2008) gave very conservative load predictions. Yu et al. (Yu et al., 2017) examined the effect of the side venting position in a pipeline on methane/air explosions and confirmed that the overpressure development was affected by the interaction of side and end vents. Xing et al. (Xing et al., 2020) researched into the influence of vent area and ignition position on overpressure oscillations in a large L/D ration duct, and indicated that a violent pressure oscillation occurred when the methane concentration was between 9.5 and 12.0 vol. % with small vent area. Wang et al. (Wang et al., 2022) captured the internal and external overpressures from vented hydrogen deflagration in a rectangular tube with different vent coefficients, and implied that the maximum internal overpressure was dominated by the external explosion in the case of a large vent coefficient. To summarize, there are a range of factors affecting the load characteristics and the subsequent structural response in a vented gas explosion. For example, the enclosure size and shape, vent size and activation pressure, ignition energy and location, obstacles and their configuration, mixture property, initial turbulence, temperature, and humidity all affect the load characteristics.

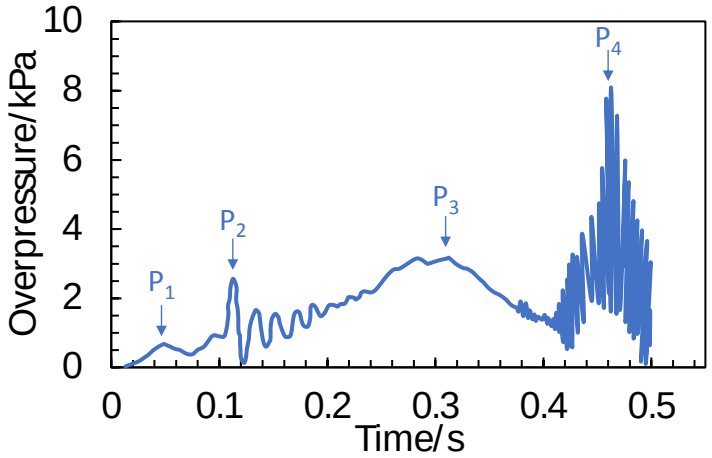

Fig. 1. A typical pressure history curve of vented gas explosion in a near-cubic vessel (Cooper et al., 1986)

Large-scale gas explosion tests are often prohibitive due to the high cost and long preparation time. With the advancement in computational mechanics, it has become possible to model complex gas combustion and explosion scenarios. For instance, the widely-recognized CFD tool FLACS, verified by a wide variety of gas explosion tests

(Arntzen, 1998; Bleyer et al., 2012; Salaun et al., 2016; Vyazmina and Jallais, 2016), is expected to yield acceptable accuracy of estimations in various gas explosion scenarios, with confinement and congestion effects at different scales. Bakke et al. (Bakke et al., 2004) utilized FLACS to explore the protection efficiency of explosion relief panels in a full-scale offshore module. Pedersen et al. (Pedersen and Middha, 2012) simulated a vented gas explosion scenario in a 64 m^3 explosion chamber using FLACS and indicated that the simulation results agreed well with experimental data and could be used for evaluating pressure loads for vented explosions. Li et al. (Li et al., 2017) employed the same CFD tool to simulate vented methane-air explosions in cylindrical enclosures, and both the peak overpressures and pressure history curves were well predicted by FLACS. Li and Hao (Li and Hao, 2018) simulated the inner and outer pressure load from a vented gas explosion tank and clarified the shortcomings of FLACS in far-field pressure prediction. Zhu et al. (Zhu et al., 2020) utilized FLACS to investigate the overpressure of methane-air explosions in a long tunnel and demonstrated that reducing the confinement was helpful to mitigate accident consequences. Lucas et al. (Lucas et al., 2021) modeled vented hydrogen explosions in 20-foot shipping containers by utilizing FLACS and concluded that this CFD tool achieved reasonable accuracy in hydrogen release, dispersion and explosion scenarios.

All vented gas explosion scenarios mentioned above had up to several vent openings which were opened in very short time intervals. This type of gas explosion, termed as a fixed vented gas explosion in this study, happened in spaces where the length, width, and height were of the same order of magnitude, and the pressure load was roughly even distributed ([d]Li et al., 2017) and sharply declined after the vent devices failure. However, in recent years, there were gas explosion accidents with much more vent openings that were damaged sequentially in a longer duration. A tragedy happened in Qingdao in 2013, which killed 62 and injured 136, was ascribed to a crude oil vapor explosion in storm drains. About 5 km of drains' covered by reinforced concrete slabs was lifted gradually in this accident (Zhu et al., 2015). Another gas explosion accident in the Kaohsiung City of China, that resulted in 32 fatalities and 321 injuries, occurred in an underground trench which blew out around 400 m of the road above the ground (Yang et al., 2016). In this kind of gas explosion, which was termed as a progressive vented gas explosion in this study, the damage process continued to propagate even though part of the confined space had been broken and the vent opening was already formed, indicating that the pressure did not decrease upon the inception of the venting process. The progressive gas explosion usually appeared in quite long confined spaces, which is quite common in city's gas supply systems. As many gas pipelines are going through underground utility tunnels (Meng et al., 2021), it is very challenging to replicate the progressive vented process in laboratory work.

In the past few years, 4 progressive vented gas explosion tests were conducted and reported in literature in 12 m and 20 m utility tunnels (Meng et al., 2020; Meng et al., 2020; Meng et al., 2021; Yang et al., 2021). This study is an extension of those studies to model the progressive vented gas explosion process by CFD simulations. First, the fixed vented gas explosions were modeled with FLACS to achieve grid convergence. Then, the numerical model of a progressive vented gas explosion with moving obstacles was established. Due to the complexity of the boundary conditions in the numerical model, an ANN-based tool was utilized to determine the key parameters so as to save computational time involved in pure numerical simulation. The experimental data were employed to ensure the accuracy of the numerical output. The results of this study promote the application of the numerical modeling of the progressive vented gas explosion in exploring gas explosion accidents and preventing their occurrence. Some shortcomings of the CFD tool FLACS were also clarified.

2 Numerical model

The CFD code FLACS was utilized to model the vented gas explosions in this study. It solves the compressible conservation equations and Reynolds Navier-Stokes equations on a 3D Cartesian grid using a finite volume method (Gexcon, 2019). Turbulence is modeled by the two-equation k-ε model (Launder and Spalding, 1974). The interaction of the reactive flow with the surrounding geometry is taken into account through a distributed porosity concept, and the k-ε model is modified to capture the impact of turbulence production from the subgrid geometry (Pedersen et al., 2013). The numerical flame is modeled by 3-5 control volumes using a so-called β-model (Arntzen, 1998).

With FLACS, objects with small displacement are modelled as rigid bodies. For those which have significant movement during the explosion process, such as moving obstacles and venting panels, FLACS can model them as pressure relief panels. In FLACS, the pressure relief panel is a 2-D rectangle with a predefined weight to imitate the inertia. By modifying the porosity in the region where the pressure relief panel is positioned, the movement of objects is simulated. The panel yield duration is determined by the panel weight and subgrid as well as the force applied to the panel (Gexcon, 2019). As shown in Table 1, several parameters are used to control the opening behavior of the pressure relief panel. There are several types of pressure relief panels provided by FLACS to simulate different deformation behavior of moving objects. For example, POPOUT is used to simulate a panel with linear displacement, whereas HINGED is utilized for rotational movement. In this study, the type of POPOUT was employed.

Table 1 Parameters controlling the opening behavior of pressure relief panel (Gexcon, 2019)

Parameter	Unit	Description
Position	m	Cartesian coordinates of the corner of the panel.
Size	m	The dimension in each of the axis directions.
Panel type	-	The type of panel to emulate different deformation behavior of moving objects. The most used types are POPOUT and HINGED.
Opening pressure differences	bar	A given value that the panel starts to yield when the net pressure over the panel exceeds it.
Initial and finial porosity	-	The initial and final porosity of the panel before and after yielding.
Weight	kg/m^2	The per unit area mass of the panel.
Drag coefficient	-	The ratio of "drag force/dynamic pressure". If the Reynolds number is high, such as in the explosion process, the drag coefficient is constant. A value 2.0 is set by the FLACS code as a fixed preset value for the panel types POPOUT and HINGE, so users do not need to input its value.
Maximum travel distance	m	The maximum travel distance is the smallest distance from the initial position of the panel to the position where the yielded panel no longer affects significantly the effective area-porosity at the initial position of the panel. For the panel types of POPOUT and HINGRD, its value is calculated from the panel subsizes, so users do not have to input its value.
Panel subsizes	m	The panel subesizes are the sizes of sub panel. The panel types of POPOUT and HINGRD are assumed to consist of sub-panels mounted on a frame.

3 Numerical simulation of fixed vented gas explosion

3.1 Experimental setup

The full-scale vented gas explosion tests with different methane concentrations, vent window designs and masonry wall designs conducted in a reinforced chamber with the internal dimensions of 3.0m×2.0m×2.0m ([a]Li et al., 2017; [b]Li et al., 2019; [c]Li et al., 2017; [d]Li et al., 2017) were taken as the numerical references. The experimental setup is presented in Fig. 2. A total of 44 overpressure history curves were collected from literature studies. Either the masonry wall or the vent window, or both of them collapsed in each test. The venting position collapsed almost at the same time, and the overpressure declined sharply following on the collapse of the masonry wall or the vent window. Details of the 44 experimental tests are listed in Table 2.

The chamber was filled with a homogeneous methane-air mixture. After the concentration of methane in the chamber reached the desired level, the fuel was ignited at the center of the chamber. The history curves obtained from each test displayed one, two or three distinct pressure peaks defined by Cooper et al. (Cooper et al., 1986) as P_1, P_2, P_3 and P_4 that are driven by different mechanisms.

Table 2 An overview of the 44 tests ([a]Li et al., 2017; [b]Li et al., 2019; [c]Li et al., 2017; [d]Li et al., 2017)

NO.	Test NO.	Masonry type	Weight kg/m^2	Boundary	Methane concentration %	Vent cover	Weight kg/m^2	P_1 kPa	Wall status	Vent window status
1	1				12.5	4 mm glass		10.76	survived	
2	2	S1	276	One-way	7.5	4 mm glass	10	13.8	survived	collapsed
3	3				7.5	4 mm glass		6.56	collapsed	
4	4	S2	276	One-way	12.5	4 mm glass	10	7.31	survived	collapsed
5	5				7.5	4 mm glass		7.56	collapsed	
6	6				12.5	4 mm glass	10	9.96	survived	
7	7	S3	276	Two-way	12.5	8 mm glass	20	39.29	survived	collapsed
8	8				7.5	4 mm glass	10	9.67	survived	
9	9				9.5	8 mm glass	20	146.5	collapsed	
10	10				11.5	6 μm film	5.5×10^{-3}	3.64	survived	
11	11	S4	132	One-way	6.5	4 mm glass	10	7.78	survived	collapsed
12	12				6.5	4 mm glass	10	10.13	collapsed	
13	13				12.5	6 μm film	5.5×10^{-3}	2.73	survived	
14	14	S5	132	One-way	12.5	4 mm glass	10	9.96	survived	collapsed
15	15				9.5	1.5 μm film	1.4×10^{-3}	1.53	collapsed	
16	16	S6	132	Two-way	≈8.5	6 μm film	5.5×10^{-3}	1.89	collapsed	collapsed
17	1				11.5	6 μm film	5.5×10^{-3}	3.77	survived	
18	2	S7	132	One-way	6.5	4 mm glass	10	7.83	survived	collapsed
19	3				6.5	4 mm glass	10	10.12	collapsed	
20	4				6.5	4 mm glass	10	10.32	survived	
21	5	S8	132	One-way	12.5	10 mm glass	25	32.79	survived	collapsed
22	6				12.5	12 mm glass	30	46.16	collapsed	
23	7				6.5	4 mm glass	10	8.73	survived	
24	8	S9	132	One-way	6.5	5 mm glass	12.5	20.93	survived	collapsed
25	9				12.5	10 mm glass	25	40.45	collapsed	
26	1				12.5	6 μm film	5.5×10^{-3}	2.91	survived	
27	2	S10	75	Two-way	12.5	4 mm glass	10	13.25	survived	collapsed
28	3				9.5	1.5 μm film	1.4×10^{-3}	85.88	collapsed	
29	4				12.5	6 μm film	5.5×10^{-3}	2.96	survived	collapsed
30	5	S11	75	Two-way	12.5	4 mm glass	10	9.27	survived	collapsed
31	6				12.5	5 mm glass	12.5	21.26	survived	collapsed
32	7				9.5	12 mm glass	30	43.17	collapsed	survived
33	8				12.5	6 μm film	5.5×10^{-3}	3.11	survived	collapsed
34	9	S12	75	Two-way	12.5	4 mm glass	10	7.57	survived	collapsed
35	10				7.5	12 mm glass	30	32.3	collapsed	survived

NO.	Test NO.	Masonry type	Weight kg/m^2	Boundary	Methane concentration %	Vent cover	Weight kg/m^2	P_1 kPa	Wall status	Vent window status
36	1				12.5	1.5 μm film	1.4×10^{-3}	0.74	survived	collapsed
37	2	S13	75	One-way	12.5	6 μm film	5.5×10^{-3}	3.84	survived	collapsed
38	3				12.5	4 mm glass	10	5.15	collapsed	survived
39	4				12.5	1.5 μm film	1.4×10^{-3}	0.37	survived	collapsed
40	5	S14	75	One-way	12.5	6 μm film	5.5×10^{-3}	2.75	survived	collapsed
41	6				9.5	12 mm glass	30	13.61	collapsed	survived
42	7				12.5	6 μm film	5.5×10^{-3}	2.91	survived	
43	8	S15	75	Two-way	12.5	4 mm glass	10	13.25	survived	collapsed
44	9				9.5	1.5 μm film	1.4×10^{-3}	1.23	collapsed	

Note: The boundary condition of one-way denotes the masonry wall was constructed with the right and left boundaries isolated from the RC frames by using plastic film. The two-way boundary denotes the masonry wall was bolted onto the RC frames along the left and right boundaries by using steel bars with an equal space of 50 cm. S1, S2, S3, S4, S5 and S6 masonry walls were all fabricated by unreinforced clay brick masonry. S1, S2 and S3 were 240 mm in wall thickness. S4, S5 and S6 were 115 mm in wall thickness. S7, S8 and S9 were constructed by clay bricks with the thickness of 115 mm. S7 was not strengthened. S8 was retrofitted by distributed carbon fiber reinforced polymer (CFRP). S9 was strengthened by concentrated CFRP. S10, S11 and S12 were fabricated by autoclaved aerated concrete (AAC) with the thickness of 120 mm. S10 was unstrengthened. S11 was rear-face strengthened by basalt fiber reinforced polymer (BFRP), and S12 was front-face strengthened by BFRP. S13, S14 and S15 were made of AAC with the thickness of 120 mm, and no strengthened method was used.

3.2 Numerical model

Fig. 2 shows the experiment and FLACS 3D geometries. The vent windows and masonry walls were modeled by the pressure relief panels. For the vent windows or masonry walls that did not experience collapse, the activation pressure was set as 999 bars, so the panels did not yield during the explosion process. For masonry walls or/and vent windows that experienced collapse deformation, the activation pressure of the panel was equal to P_1, as P_1 was always associated with the removal of the explosion relief vent panels and its magnitude was identical to or slightly greater than the activation pressure of the vent panel (Pedersen et al., 2013).

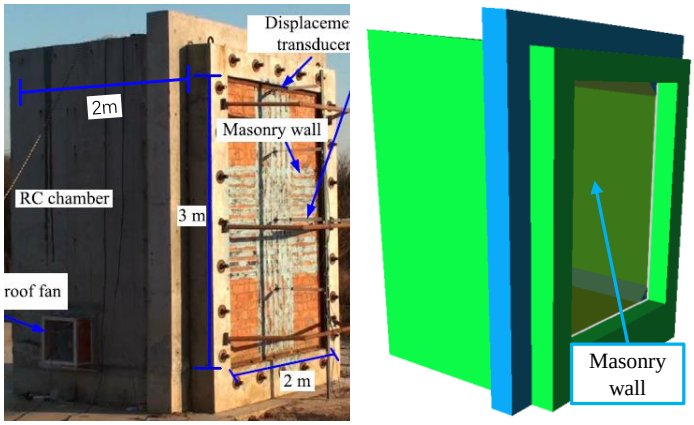

(a) Side view

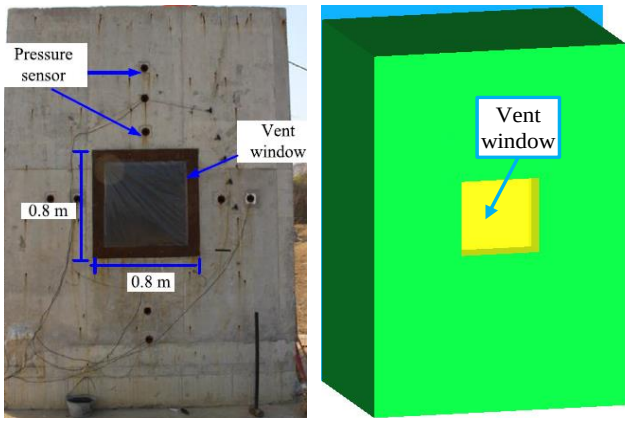

(b) Back view

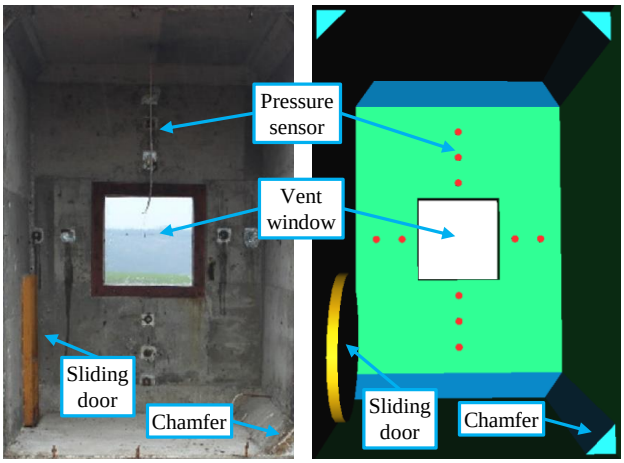

(c) Internal view

Fig. 2. Details of the experiment ([b]Li et al., 2019) (left) and FLACS 3D geometries (right).

For all simulations, the initial pressure and temperature were 1 bar and 20 ℃, respectively. All the objects excluding the vent window and collapsed masonry wall were modeled as rigid. The boundary condition of Z^- was EULER to model the reflection effect of the ground, whereas the other 5 directions of boundary conditions were PLANE_WAVE to eliminate the pressure wave reflection. As shown in Fig. 3, grid cells in the chamber region were modeled cubically. To reduce boundary influences and computational difficulty, the grid region was stretched to 2 times larger in the X^+ and X^- direction, 4 times in the Z^+ direction and 10 times in the Y^+ (vent) direction. For the scenarios where the masonry walls experienced collapse, Y^- was also extended to 10 times larger. The percentage difference of the grid was retained below 30%. CFLC and CFLV, which were used for controlling the time step, were set as 5 and 0.5 (Gexcon, 2019).

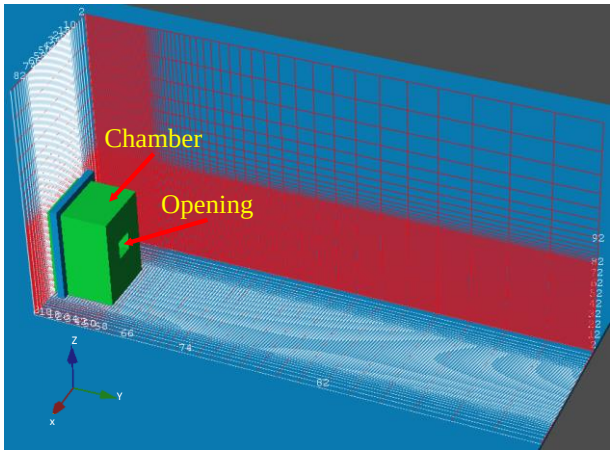

Fig. 3. Computational domain for the chamber gas explosion.

3. 3 Grid independent study

A grid resolution of 10 cm, 5 cm and 4 cm in the chamber region was tested to explore the grid independence. The simulation parameters were set in line with Test 2 conducted by Li et al. ([b]Li et al., 2019). The simulation was performed on a computer with the CPU

of Intel i9-10900 5.2 GHz, and the memory size of 32 GB. A single core was used for each case.

As shown in Fig.4, only P_1 was captured in this experiment, since the pressure curve presented one dominant peak. A grid resolution of 5 cm was necessary since a grid resolution of 10 cm produced a slower rate of pressure rise. The results produced by the 4 cm grid did not show a significant difference with 5 cm resolution. Table 3 presents more details of the results from the different grid sizes. The computational time of the 4 cm grid was about 2 times longer than that of the 5 cm grid size. At the same time, owing to the typical treatment between the propagation of the reacting zone and the flow equations, smaller grid sizes may not necessarily achieve better results. For a grid size of 1-2 cm or less, the subgrid model for premixed combustion was not applicable and the burning velocities tended to be severely overpredicted (Gexcon, 2019). Thus, a 5 cm grid size in the fuel region was employed throughout the study.

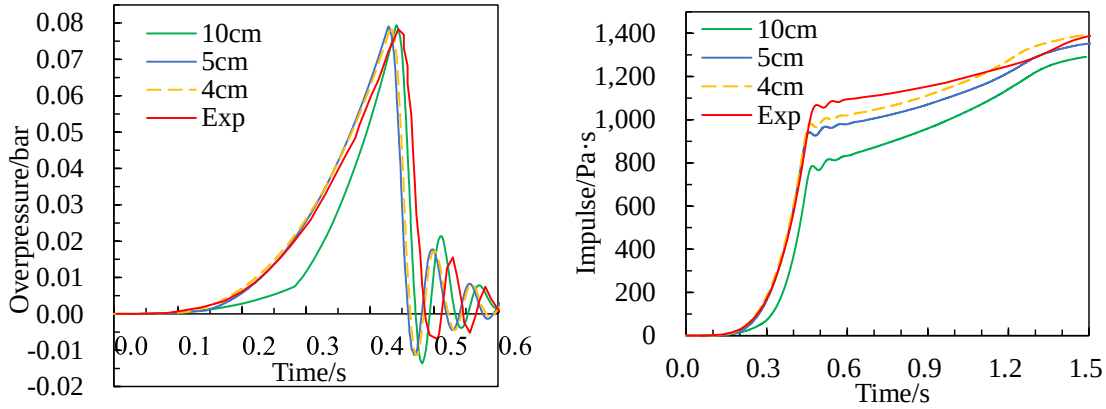

(a) Overpressure history curve (b) Impulse history curve

Fig. 4. Grid cell size dependence of the numerical results ([b]Li et al., 2019).

Table 3 Grid cell size dependence and comparison between numerical and experimental results

Grid size /cm	10	5	4	Experimental value
Peak pressure/kPa	7.94	7.91	7.91	7.83
Error/%	1.40%	1.02%	1.02%	/
Peak impulse/Pa·s	1291	1355	1368	1430
Error/%	-9.72%	-5.24%	-4.34%	/
Cell number	13.9×10^4	72.3×10^4	123.4×10^4	/
Computational time/h	0.61	7.31	15.26	/

3.4 Experimental and numerical result comparison

Up to 3 pressure peaks were captured in each test. As shown in Fig. 5, P_1, P_2 and P_3 were reproduced numerically, and the numerical and experimental curves approximately coincided with each other. However, the model did not yield P_4 generated from the interaction between the flame and acoustic wave (Cooper et al., 1986) as the flame-acoustic interaction is not modeled (Pedersen and Middha, 2012).

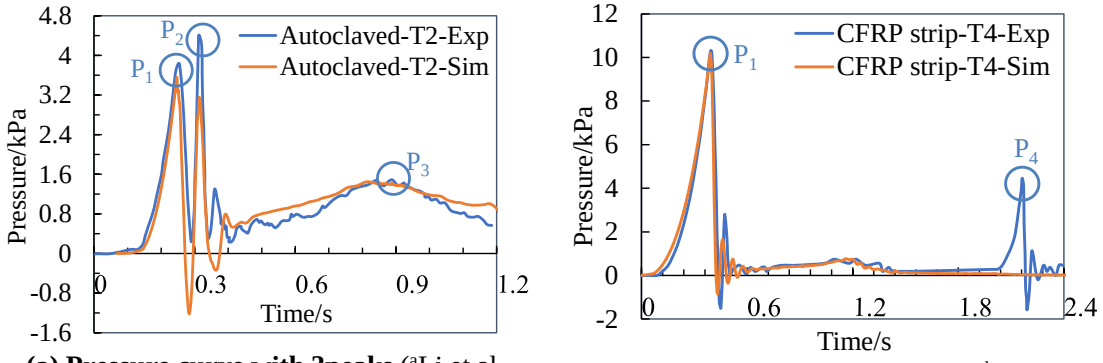

(a) Pressure curve with 3peaks ([a]Li et al., 2017) **(b) Pressure curves with 2 peaks** ([b]Li et al., 2019)

Fig. 5. Overpressure history comparison of multiple overpressure peak curves.

Fig. 6 displays the 44 respective peaks (P_1, P_2 and P_3) collected from literature and compared with the numerical results. The findings revealed that FLACS predicted P_1 accurately within the error of 30%. By comparison, the numerical results of P_2 and P_3 were less accurate.

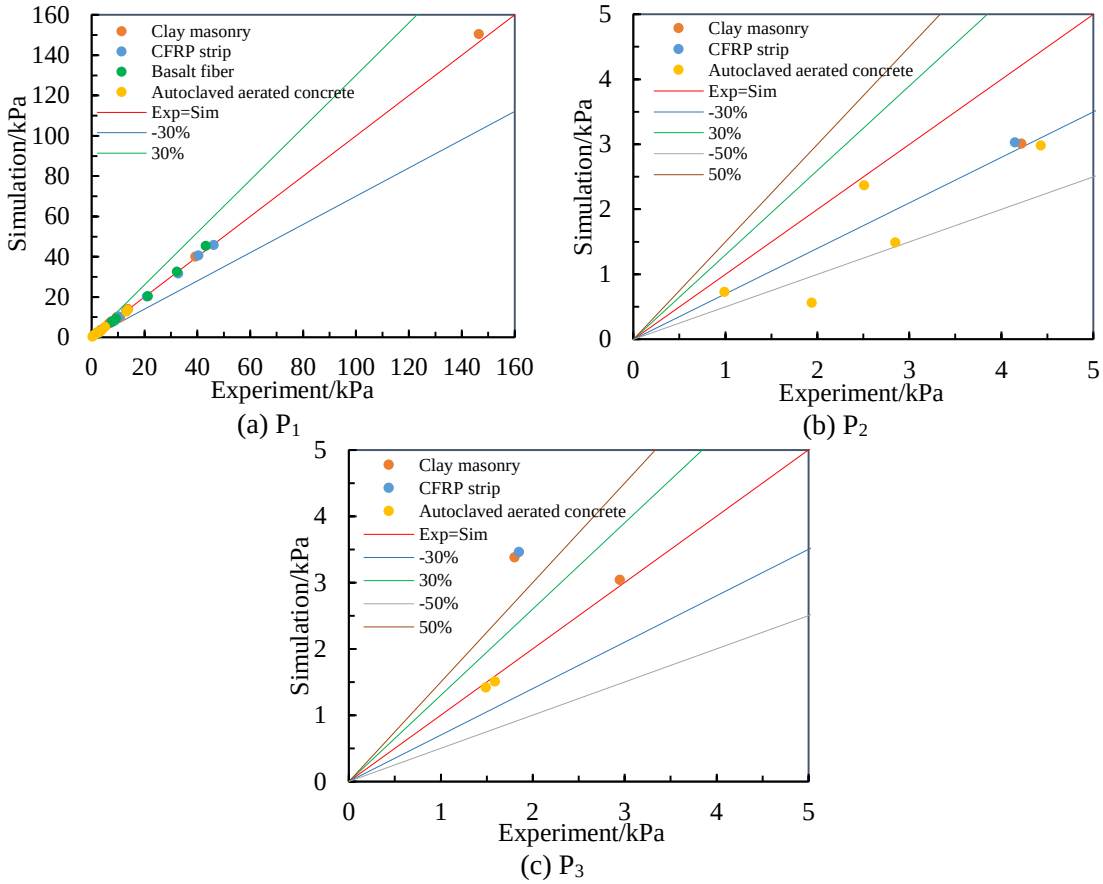

(a) P_1 (b) P_2 (c) P_3

Fig. 6. Experimental and numerical results of overpressure peaks ([a]Li et al., 2017; [b]Li et al., 2019; [c]Li et al., 2017; [d]Li et al., 2017).

The difference between the numerical and experimental results comes from both experimental and numerical aspects. The experimental uncertainty is always existing and can be up to ±50% for repeated tests in vented gas explosion tests (Pedersen and Middha,

2012). As mentioned before, the magnitude of P_1 was identical to or slightly greater than the activation pressure of the vent panel, and P_1 was set as the activation pressure in the numerical model, explaining why P_1 was more accurate compared to P_2 and P_3. Also, FLACS uses a simplified method to model the process of the removal of vent devices. FLACS changes the porosity where the panel is occupied initially but does not trace the movement of the panel. This simplification does not influence P_1 too much as it occurs prior to the panel failure. But this simplification will have a more visual impact on P_2 and P_3 owing to their occurrence after panel failure.

4 Numerical simulation of progressive vented gas explosion

4.1 Experimental setup

A series of full-scale gas explosion tests in a buried tunnel with progressive vent openings and moving obstacles were performed (Meng et al., 2020; Meng et al., 2021; Yang et al., 2021). In this study, the experimental results from Yang's study were selected and compared numerically.

As shown in Fig. 7, the experiment was conducted in a tunnel with dimensions of 0.6 m deep, 1.6 m wide and 20 m long. Because the length of the tunnel was significantly larger than that of depth and width, the pressure load in the tunnel was uneven and the venting covers over the tunnel were lifted one by one during the experiment. The wooden and steel obstacles were placed at the bottom of the tunnel with a spacing of 1 m to increase the turbulence and hence boost the overpressure. The concrete slab specimens were fully constrained by metal fixings at one end of the tunnel away from the ignition point. Except for the concrete slabs, the remaining top cover slabs were made of steel, which were supported by the tunnel and fixed by sandbags. 420 sandbags weighing 25 kg each were evenly placed on the steel slabs. Furthermore, the steel slabs were connected using a square steel tube. All the gaps among the slabs were filled with expandable foam to seal the tunnel. The concentration of methane was 9.5%, and the ignition point was at the opposite end of the concrete slab specimens.

To model aforementioned experimental scenario, the main challenge came from the multi-vent openings along the tunnel length and the moving obstacles inside the tunnel. The first challenge was to model the lifting process of the steel slabs. Unlike a fixed vented gas explosion in which the venting panels damaged at relatively constant pressure and short duration, the relief pressure for the progressive vented explosion in the experimental scenario was more difficult to estimate as the expandable foam among the gaps and the square tube connected with the steel slabs gave much uncertainty. The steel slabs were lifted one by one, indicating that it was not a fixed pressure when the slabs

were blown up. What is more, during the process of lifting from the tunnel top, the steel slabs still contributed to the confined space of the tunnel, so it was unclear whether the period after the steel slabs were lifted away from the tunnel top should be taken into consideration. Also, to what extent the falling process of the steel slabs affected the explosion process was unclear. Another difficulty was modeling the moving obstacles inside the tunnel. These obstacles should be taken into account at the early stage of the explosion process but could be ignored when the explosion process developed into a certain phase when these obstacles were displaced to one end of the tunnel or even blown out of the tunnel. CFD simulations in combination with correlation analysis and an artificial neural network (ANN) were utilized to overcome these challenges.

4.2 Modelling progressive vented gas explosion

Typically, the activation pressure of the pressure relief panels was predetermined as the value when the panel started to be removed. A numerical model was established to verify its applicability for a progressive vented gas explosion.

4.2.1 Numerical model

As shown in Fig. 7, the tunnel walls, concrete specimen covers and the tube were modeled as rigid bodies. The obstacles inside the tunnel were modeled as pressure relief panels having the identical width and height as the real obstacles. The computational domain was stretched to reduce boundary influence.

The activation pressure of the steel slabs and the obstacles' activation pressure were the critical parameters in the numerical model. The initial activation pressures of the obstacles were estimated as:

$$x_{1(2)}\, s_{1(2)} > \mu_{1(2)}{}' N_{1(2)} \tag{2}$$

where x_1 is the activation pressure of the wooden obstacles; x_2 is the activation pressure of the steel obstacles; $s_{1(2)}$ is the area of the pressure relief panels, m^2; $\mu_{1(2)}$ is the friction coefficient between the wooden (steel) and the tunnel bottom; $N_{1(2)}$ is the gravity of each wooden (steel) obstacle, N.

The densities of wooden and steel were 600 kg/m^3 and 7850 kg/m^3, respectively, and the volumes of each wooden and steel obstacle were 2.88×10^{-3} m^3 and 6.72×10^{-4} m^3, so N_1 and N_2 were 19.6 N and 51.7 N. μ_1 and μ_2 were estimated as 0.8 and 0.65, respectively (Jaaranen and Fink, 2020; Rabbat et al., 1985). Hence, the values of x_1 and x_2 were estimated as 4.7×10^{-4} bar and 2.5×10^{-3} bar, respectively.

When the inner pressure exceeded the gravity force of the steel slabs, the slabs over the tunnel started to move. This inner pressure was denoted by x_3 here. The weight of each slab (including the weight of sandbags above it) was around 252.4 kg. Hence, x_3 was estimated to be 3.9×10^{-2} bar. There were expandable foam and rubber among the steel slab gaps, and square steel tubes connecting the steel plates together, which provided additional drag forces to the steel slabs, so x_3 must be greater than 3.9×10^{-2} bar, here x_3 was multiplied by 1.5, and the final value for x_3 was 5.8×10^{-2} bar.

(a) Arrangement of obstacles

(b) Experimental site setup

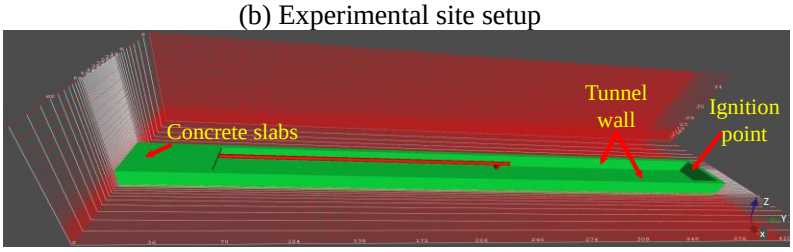

(c) Geometry model and computational grid

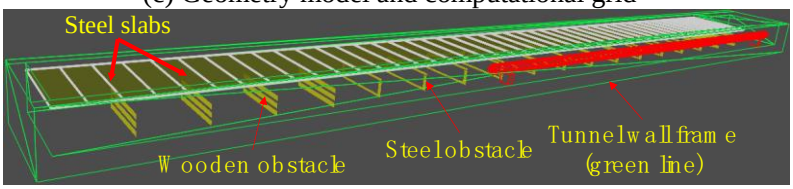

(d) The pressure relief panels' position

Fig.7 Details of experimental setup and numerical geometry

4.2.2 Numerical result

The predicted pressure curve is presented in Fig. 8. The peak pressures at positions #1 and #2 were 0.088 bar and 0.086 bar, respectively, which were far lower than the experimental values of 3.15 bar and 2.37 bar. The pressure duration was also much shorter than the experimental one (as shown in Fig. 10). The results revealed that the typical method suitable for modeling the fixed vented gas explosion is inappropriate for a progressive vented gas explosion. The model only changes the porosity in the region where the pressure relief panel is positioned. Consequently, the tunnel began to turn into an open space when the inner overpressure overcame the gravity of the steel slabs. However, in the real situation, when the inner overpressure overcame the gravity of the steel slabs, the slabs just initiated the movement with an increasing velocity from 0 m/s. There was still 0.1 m to go before the slabs were lifted over the tunnel top. During this period, the steel slabs and the tunnel wall altogether could still be considered as a confined space, and the overpressure would increase dramatically in such a space. Therefore, the typical method used to model the progressive vented gas explosion caused the premature opening of the tunnel cover and resulted in a lower overpressure assessment.

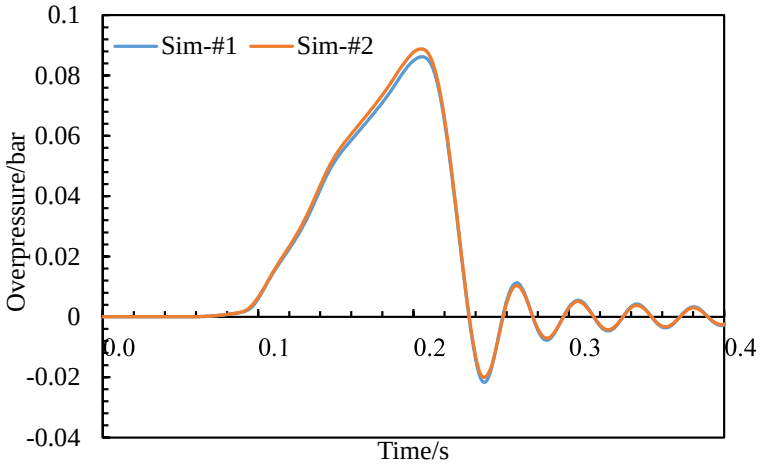

Fig. 8. The numerical result based on the typical method

4.3 The modified method in modelling progressive vented gas explosion

4.3.1 Numerical model

Based on the high-speed video images that recorded the experimental process, the steel slabs were lifted to about 0.8 m above the tunnel top. The high-speed video images also showed that there was a persistent interaction between the steel slabs and the flame when the steel slabs were lifting, indicating that the pressure relief process might last for the whole lifting process of the steel slabs. Hence, the steel slab cover was modeled as 10 layers of pressure relief panels with the top layer 0.8 m away from the tunnel top to simulate the dynamic lifting process of the steel slabs (Fig. 9). Each layer consisted of 44 panels with dimensions of 0.4 m wide and 1.6 m long which was identical to the real steel slabs. The distance between 2 layers of panels was set as 0.1 m. The bottom 2 layers of pressure relief panels were inside the tunnel as the upper tunnel wall from 0.6 m to 0.7 m was used to place the concrete specimens and steel slabs. The overall number of pressure relief panels in the established numerical model was 506.

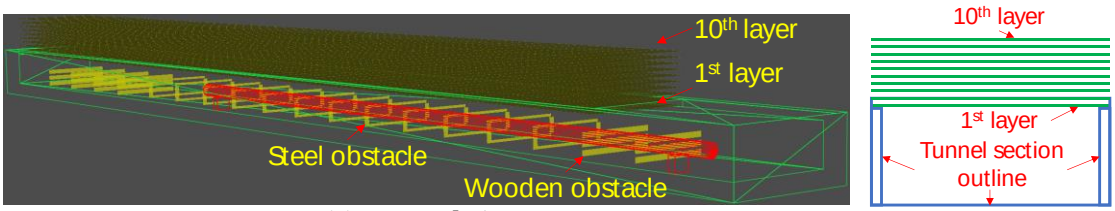

(a) General view **(b) Section view**

Fig. 9. Details of the pressure relief panels.

4.3.2 Mathematical model and solving procedure

For the numerical model, the initial and boundary conditions need to be known. A few parameters, such as the layout of the tunnel, the weight of obstacles, steel slabs and sandbags, the methane concentration, and the initial temperature could be obtained directly from the experimental setup. The main challenge was to determine the activation pressure of the steel slabs over the tunnel and the obstacles' activation pressure. Numerous simulations might be needed to replicate the experimental results, as 506 activation pressures of pressure relief panels were needed to be determined in theory. Hence, an ANN-based tool was utilized to substitute the simulation process with limited numerical data as the training data aiming to save a large amount of computational time involved in pure numerical simulation.

A mathematical model involving the activation pressures was established to help implement the ANN tool. To describe and solve the model efficiently, assumptions were made as follows: (1) Each wooden and steel obstacle had the same activation pressure, respectively. (2) The steel slabs only moved in the vertical direction, and the rotation of each slab was neglected. (3) The tunnel walls and concrete slabs were considered as rigid bodies. (4) It was the ascending, not the descending process of the steel slabs that dominated the pressure characteristics. Excluding the foregoing 4 assumptions, each layer of pressure relief panels above the tunnel having the identical activation pressure was assumed at first. Based on these assumptions, the problem can be characterized as:

$$f(x_1, x_2, \ldots, x_{12})=(y_1, y_2) \quad (1)$$

where x_1 is the activation pressure of wooden obstacles, x_2 is the activation pressure of steel obstacles, x_3 to x_{12} are the activation pressures from the 1st to 10th layer of the pressure relief panels above the tunnel, and y_1 is the arithmetic mean value of peak pressure of positions #1 and #2 in the experiment (see Fig. 10). y_2 is the arithmetic mean value of the peak impulse of positions #1 and #2 in the experiment. Since positions #1 and #2 were close (0.4 m away from each other), and their pressure history curves were similar in trend and shape, the arithmetic mean of the 2 positions was used to reduce the number of variables and alleviate the difficulty in solving the mathematical model. Hence, y_1=2.76 bar, y_2=37942 Pa·s. As shown in Fig. 10, the pressure period that caused the deformation of concrete slabs is $\triangle P_2$, so the main purpose is to reproduce $\triangle P_2$. The shape of $\triangle P_2$ can be approximately simplified as a triangle. y_1 is the height of the triangle, and y_2 is the area of the triangle. When y_1 and y_2 were determined, the duration of $\triangle P_2$ was determined.

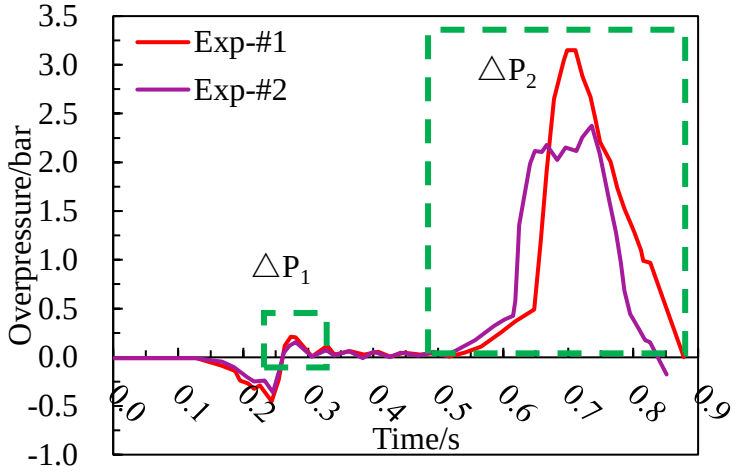

Fig. 10. The overpressure curves at #1 and #2 positions.

The initial values of x_1, x_2 and x_3 were estimated using the typical method for the fixed vented gas explosion and the values were 4.7×10^{-4}, 2.5×10^{-3} and 5.8×10^{-2} bar, respectively. They were going to be adjusted to proper values through the procedure presented in Fig. 10. The values of x_4 to x_{12} were totally blind and no available evidence could be used to assess their values, so they were estimated.

The following procedure was proposed to solve this mathematical model. Even with the assumption that each layer of the pressure relief panels had the same activation pressure, numerous simulations were needed to be tried when every potential solution was tested, as the potential combinations of activation pressures were still large. Here an optimized procedure was proposed to diminish the variables, decrease the numerical simulation time and finally simplify the process. As shown in Fig. 11, correlation analysis was conducted to exclude non-key variables, and ANN was utilized to replace the numerical simulation process to filter the solutions that were inconsistent with the experimental results.

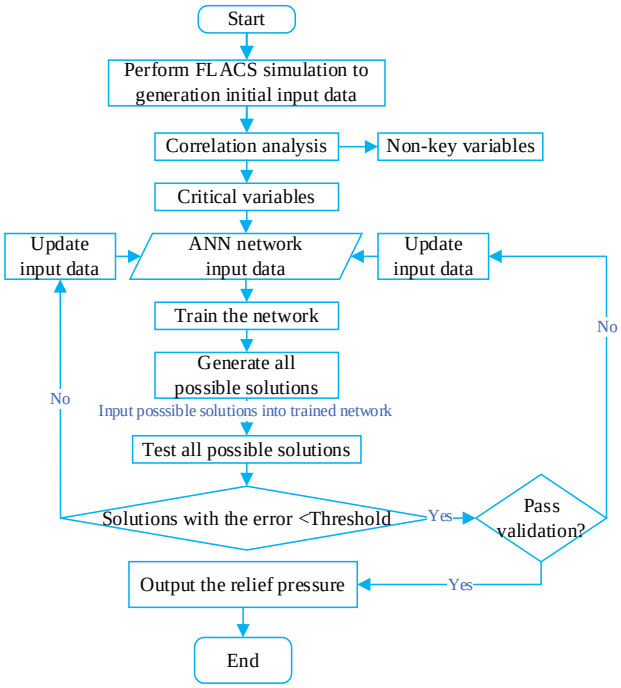

Fig. 11. Flow chart of solving the ANN-numerical hybrid model.

At first, some initial input data were generated. Different values and combinations of x_1 to x_{12} were chosen randomly. Subsequently the corresponding simulation results were obtained through numerical simulation. Based on the numerical results and corresponding x_1 to x_{12}, the correlation coefficient among the activation pressure of the pressure relief panels and peak pressure as well as peak impulse can be calculated. Here, the Pearson correlation coefficient (Fu et al., 2020) was calculated through Eq. (3).

$$r(x,y)=\frac{\sum_{i=1}^{n}\left[(x_i-\bar{x})\cdot(y_i-\bar{y})\right]}{\sqrt{\sum_{i=1}^{n}(x_i-\bar{x})^2}\cdot\sqrt{\sum_{i=1}^{n}(y_i-\bar{y})^2}} \tag{3}$$

where $r(x,y)$ is the correlation coefficient between x and y. The closer the value is to +1 or -1, the stronger the correlation. x represents x_1 to x_{12}. y represents y_1 and y_2. n refers to the sample number of input data. $\bar{x}$ and $\bar{y}$ denote the mean values of the two variables. It is generally known that $0.6\leqslant r(x,y)<0.8$ represents high correlations, and $r(x,y)>0.8$ represents very high correlations. These variables with relatively low correlations were known as non-key variables, which would be excluded from the following numerical model, while those with relatively high correlations were defined as critical variables.

Then, ANN was employed to fit the variables and corresponding results. A typical backpropagation neural network with 1 input layer, 1 hidden layer and 1 output layer was

used. The topology of the BP (backpropagation) neural network is shown in Fig. 12. The detailed theory can be found in the literature (Li et al., 2012), here the critical parameters employed in the present study were illustrated. The fractions of samples employed for training and testing are 90% and 10%, respectively. The number of hidden neurons is 10. The activation functions used in the hidden layer and output layer are tansig(x) and purelin(x), respectively. The network training function is trainlm (Levenberg-Marquardt backpropagation). The backpropagation neural network is implemented by using the machine learning toolbox in MATLAB R2018a. The maximum training epochs, the training goal and the training rate are 5000, 10^{-5} and 10^{-2}, respectively. The code used in the present study was uploaded to GitHub (Chen, 2022).

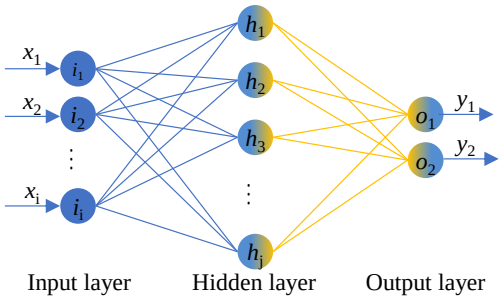

Fig. 12. Structure of the backpropagation neural network.

After the BP neural network finished training, it was employed to yield the outcome of the input data in a much wider range. In this study, 4 level nested loops were utilized to generate all possible combinations of activation pressure of the pressure relief panels. When the error as compared to the experimental results reached a certain threshold, the search stopped and the solutions were output. Of course, this step could be done by numerical simulation, but it would cost much longer time. For example, about 8 hours are needed to finish each single case by performing FLACS at the authors' computer (Intel i9-10900, 5.2 GHz, 32 GB), but only several minutes are needed to test hundreds of solutions with reasonable accuracy when the backpropagation neural network is used. Hence, the neural network is an efficient tool to search for potential solutions in a short time.

Finally, the potential solutions identified by the trained network were validated through FLACS and experimental results. First, FLACS used the corresponding input variables to yield the pressure history curves. Then, these curves were compared with the experimental results to examine whether the numerical results fit with the experimental data. As the numerical results were acceptable, the solving process went to an end. When not, then the numerical results were added to the input data bank of the neural network,

and the network retrained again. As the trained network could not find any satisfying solution, more random numerical solutions were performed to enrich the input data bank.

4.4 Correlation analysis

48 scenarios were simulated. The details of each scenario and numerical results are presented in Table 4. x_1 and x_2 represent the activation pressure of the obstacles inside the tunnel, and it is unreasonable to exclude them from the numerical model as the obstacles have significant impact on load characteristics deriving from gas explosion. Therefore, here only the correlation coefficients among x_3 to x_{12} and y_1, y_2 were calculated.

Table 4. The random numerical simulation results

NO.	x_1 bar	x_2 bar	x_3 bar	x_4 bar	x_5 Bar	x_6 bar	x_7 bar	x_8 bar	x_9 bar	x_{10} bar	x_{11} bar	x_{12} bar	y_1 bar	y_2 Pa • s	Note
1	0.0	0.0	0.00	0.00	0.00	0.00	0.00	0.00	0.00	0.00	0.00	0.00	0.00	12	without obstacles and steel slabs
2	0.0	0.0	5.00	5.00	5.00	5.00	5.00	5.00	5.00	5.00	5.00	5.00	5.31	114842	with steel slabs which had fixed activation pressures and without obstacles
3	6.9×10^{-2}	6.9×10^{-2}	0.00	0.00	0.00	0.00	0.00	0.00	0.00	0.00	0.00	0.00	0.01	13	with obstacles and without steel slabs
4	6.9×10^{-2}	6.9×10^{-2}	5.00	5.00	5.00	5.00	5.00	5.00	5.00	5.00	5.00	5.00	7.76	33459	with obstacles and steel slabs which had fixed activation pressures
5	1.0×10^{-2}	1.0×10^{-2}	1.00	1.00	1.00	1.00	1.00	1.00	1.00	1.00	1.00	1.00	4.12	9754	
6	0.0	6.9×10^{-2}	1.00	1.00	1.00	1.00	1.00	1.00	1.00	1.00	1.00	1.00	3.68	12721	
7	3.3×10^{-3}	1.0×10^{-2}	0.04	1.00	0.88	0.76	0.64	0.52	0.40	0.28	0.16	0.04	1.88	8894	
8	4.7×10^{-4}	2.5×10^{-3}	0.04	2.00	1.76	1.51	1.26	1.02	0.77	0.53	0.28	0.04	2.54	21326	
9	4.7×10^{-4}	2.5×10^{-3}	0.06	3.00	1.00	0.33	0.11	0.04	0.01	0.00	0.00	0.00	3.64	34351	
10	4.7×10^{-4}	2.5×10^{-3}	0.06	4.00	1.33	0.44	0.15	0.05	0.02	0.01	0.00	0.00	4.20	48059	
11	4.7×10^{-4}	2.5×10^{-3}	0.06	5.00	1.67	0.56	0.19	0.06	0.02	0.01	0.00	0.00	5.20	59389	
12	3.3×10^{-3}	1.0×10^{-2}	0.04	0.52	1.00	0.86	0.73	0.59	0.45	0.31	0.18	0.04	1.18	5883	
13	4.7×10^{-4}	2.5×10^{-3}	0.04	1.02	2.00	1.72	1.44	1.16	0.88	0.60	0.32	0.04	1.24	8864	
14	4.7×10^{-4}	2.5×10^{-3}	0.06	1.00	3.00	1.00	0.33	0.11	0.04	0.01	0.00	0.00	1.23	8735	
15	4.7×10^{-4}	2.5×10^{-3}	0.06	1.33	4.00	1.33	0.44	0.15	0.05	0.02	0.01	0.00	1.44	11883	
16	4.7×10^{-4}	2.5×10^{-3}	0.06	1.67	5.00	1.67	0.56	0.19	0.06	0.02	0.01	0.00	2.20	18042	
17	3.3×10^{-3}	1.0×10^{-2}	0.06	0.36	0.68	1.00	0.84	0.68	0.52	0.36	0.20	0.04	0.84	4629	
18	4.7×10^{-4}	2.5×10^{-3}	0.06	0.69	1.35	2.00	1.67	1.35	1.02	0.69	0.37	0.04	1.11	6546	
19	4.7×10^{-4}	2.5×10^{-3}	0.06	0.33	1.00	3.00	1.00	0.33	0.11	0.04	0.01	0.00	0.75	4193	with obstacles and steel slabs which had increasing then decreasing activation pressures
20	4.7×10^{-4}	2.5×10^{-3}	0.06	0.44	1.33	4.00	1.33	0.44	0.15	0.05	0.02	0.01	0.91	4600	
21	4.7×10^{-4}	2.5×10^{-3}	0.06	0.56	1.67	5.00	1.67	0.56	0.19	0.06	0.02	0.01	1.02	5444	
22	3.3×10^{-3}	1.0×10^{-2}	0.06	0.28	0.52	0.76	1.00	0.81	0.62	0.42	0.23	0.04	0.69	4053	
23	4.7×10^{-4}	2.5×10^{-3}	0.06	0.53	1.02	1.51	2.00	1.61	1.22	0.82	0.43	0.04	0.99	4914	
24	4.7×10^{-4}	2.5×10^{-3}	0.06	0.11	0.33	1.00	3.00	1.00	0.33	0.11	0.04	0.01	0.19	2738	
25	4.7×10^{-4}	2.5×10^{-3}	0.06	0.15	0.44	1.33	4.00	1.33	0.44	0.15	0.05	0.02	0.25	3251	
26	4.7×10^{-4}	2.5×10^{-3}	0.06	0.19	0.56	1.67	5.00	1.67	0.56	0.19	0.06	0.02	0.33	3504	
27	3.3×10^{-3}	1.0×10^{-2}	0.06	0.23	0.42	0.62	0.81	1.00	0.76	0.52	0.28	0.04	0.61	3797	
28	4.7×10^{-4}	2.5×10^{-3}	0.06	0.43	0.82	1.22	1.61	2.00	1.51	1.02	0.53	0.04	0.89	4442	
29	4.7×10^{-4}	2.5×10^{-3}	0.06	0.17	0.52	0.75	1.00	3.00	1.00	0.33	0.11	0.04	0.30	3425	
30	4.7×10^{-4}	2.5×10^{-3}	0.06	0.17	0.52	1.57	2.80	4.00	1.33	0.44	0.15	0.05	0.30	3425	
31	4.7×10^{-4}	2.5×10^{-3}	0.06	0.10	0.19	0.56	1.67	5.00	1.67	0.56	0.19	0.06	0.18	2623	
32	3.3×10^{-3}	1.0×10^{-2}	0.06	0.20	0.36	0.52	0.68	0.84	1.00	0.68	0.36	0.04	0.55	3601	

NO.	x_1 bar	x_2 bar	x_3 bar	x_4 bar	x_5 Bar	x_6 bar	x_7 bar	x_8 bar	x_9 bar	x_{10} bar	x_{11} bar	x_{12} bar	y_1 bar	y_2 Pa • s	Note
33	4.7×10^{-4}	2.5×10^{-3}	0.06	0.37	0.69	1.02	1.35	1.67	2.00	1.35	0.69	0.04	0.80	4179	
34	4.7×10^{-4}	2.5×10^{-3}	0.06	0.10	0.18	0.31	0.54	0.95	3.00	1.00	0.33	0.11	0.18	2624	
35	4.7×10^{-4}	2.5×10^{-3}	0.06	0.12	0.23	0.46	0.93	1.86	4.00	1.33	0.44	0.15	0.20	2794	
36	4.7×10^{-4}	2.5×10^{-3}	0.06	0.11	0.22	0.43	0.84	1.64	5.00	1.67	0.56	0.19	0.20	2760	
37	3.3×10^{-3}	1.0×10^{-2}	0.06	0.18	0.31	0.45	0.59	0.73	0.86	1.00	0.52	0.04	0.51	3440	
38	4.7×10^{-4}	2.5×10^{-3}	0.06	0.32	0.60	0.88	1.16	1.44	1.72	2.00	1.02	0.04	0.72	4000	
39	4.7×10^{-4}	2.5×10^{-3}	0.06	0.10	0.17	0.29	0.48	0.82	1.40	3.00	1.00	0.33	0.18	2621	
40	4.7×10^{-4}	2.5×10^{-3}	0.06	0.10	0.18	0.31	0.54	0.95	1.67	4.00	1.33	0.44	0.18	2624	
41	4.7×10^{-4}	2.5×10^{-3}	0.06	0.10	0.18	0.31	0.54	0.95	1.67	5.00	1.67	0.56	0.18	2624	
42	3.3×10^{-3}	1.0×10^{-2}	0.06	0.16	0.28	0.40	0.52	0.64	0.76	0.88	1.00	0.04	0.47	3328	
43	4.7×10^{-4}	2.5×10^{-3}	0.06	0.28	0.53	0.77	1.02	1.27	1.51	1.76	2.00	0.04	0.65	3820	
44	4.7×10^{-4}	2.5×10^{-3}	0.06	0.09	0.15	0.24	0.38	0.61	0.97	1.56	3.00	1.00	0.18	2608	
45	4.7×10^{-4}	2.5×10^{-3}	0.06	0.09	0.15	0.24	0.38	0.61	0.97	1.56	4.00	1.33	0.18	2608	
46	4.7×10^{-4}	2.5×10^{-3}	0.06	0.09	0.15	0.24	0.39	0.64	1.03	1.66	5.00	1.67	0.18	2610	
47	4.7×10^{-4}	2.5×10^{-3}	0.06	2.50	0.83	0.28	0.09	0.03	0.01	0.00	0.00	0.00	2.76	26644	
48	4.7×10^{-4}	2.5×10^{-3}	0.06	3.00	0.00	0.00	0.00	0.00	0.00	0.00	0.00	0.00	3.63	33765	with 2 layers of steel slabs which had fixed activation pressures

The correlation coefficient results are shown in Fig. 13. x_3 and x_4 exhibited the highest correlation with y_1 and y_2 as compared to other layers of activation pressures. It is noticed that x_3 and x_4 are the activation pressure of two layers of the pressure relief panels inside the tunnel.

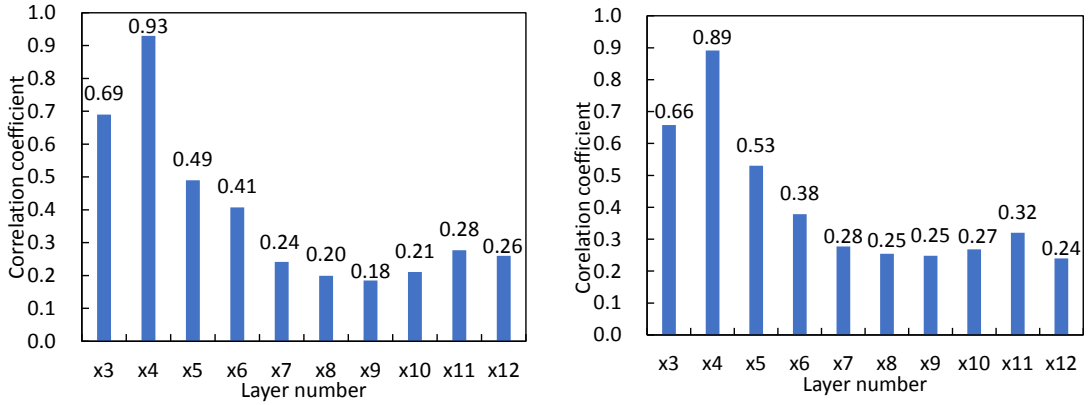

(a) Peak pressure (b) Impulse

Fig. 13. Correlation coefficients between peak pressure/impulse and activation pressure of each layer.

Fig. 14 presents a comparison of the numerical results at 2, 3 and 10 layers of the pressure relief panels above the tunnel. The pressure history curves were quite similar in shape, and the peak impulse with 2 layers was slightly lower than that of 10 layers. Thus, in the following analysis, x_5 to x_{12} were excluded from the numerical model to simplify the solving process. The correlation analysis results revealed that the steel slabs had insignificant impact on the progressive vented gas explosion load after being lifted above the tunnel top.

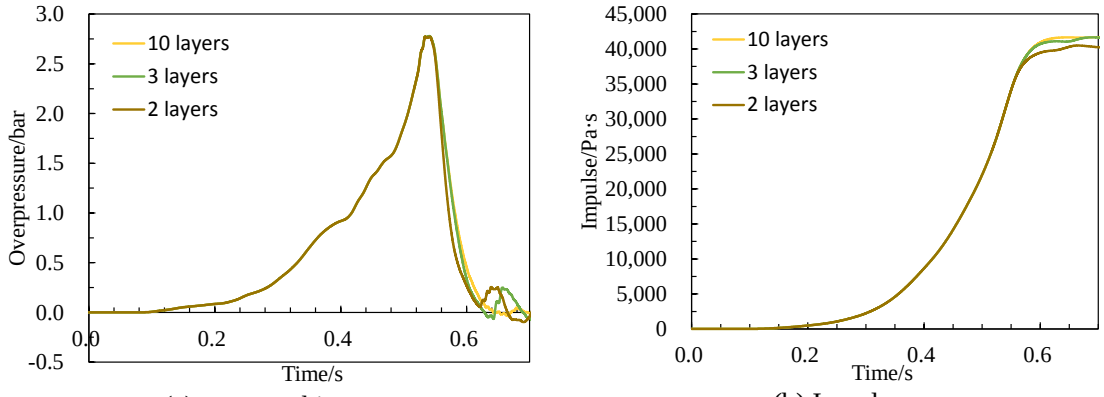

(a) pressure history (b) Impulse

Fig. 14. Result comparison between 2,3 and 10 layers of pressure relief panels.

From the random simulation it follows that the assumption of each layer of the pressure relief panels having the same activation pressure is unreasonable. As shown in Fig. 15, the numerical results indicated that the first venting position was not at the ignition end. But in the experiment, the steel slabs were blown upwards one by one from the ignition

end to the concrete specimen end. The reason for this is that in the actual scenario, the steel slab at the ignition side had the slightest drag force since only one side of the slab was connected with its neighboring slab. By comparison, two sides were connected for these steel slabs that were not placed at the two ends of the tunnel, and an additional frictional force was provided by the concrete specimen for the steel slab adjacent to the concrete. However, for numerical simulation, the activation pressure for the 2nd layer pressure panel was the same, and the panel was opened at the position where the peak pressure reached the predetermined activation pressure. To assess this progressive opening procedure correctly, in the subsequent simulations, the activation pressures of the panels were considered as lower at the ignition end and higher at the other end.

(a) Experimental venting position

(b) Numerical venting position

Fig. 15. Comparison between the experimental and numerical vented positions in the condition that the 2nd layer of pressure relief panels has the same activation pressure.

The correlation analysis and simulation results revealed that x_5 to x_{12} could be excluded from the subsequent numerical model, and the activation pressures for the 2nd layer of pressure relief panels should increase for the panel from the ignition end to the other end of the tunnel. Here, a linear ascent trend was assumed. The numerical model was simplified as shown in Fig. 16 and the mathematical model of Eq. (1) was simplified to:

$$f(x_1, x_2, x_3, x_{4,1}, x_{4,44})=(y_1, y_2) \quad (4)$$

where $x_{4,1}$ represents the activation pressure of the pressure relief panel close to the ignition end, and $x_{4,44}$ represents the activation pressure of the pressure relief panel close to the concrete specimen.

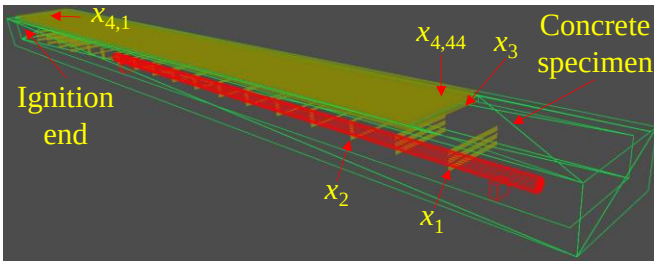

Fig. 16. The simplified numerical model

4.5 ANN-based prediction results

4.5.1 Obstacles with calculated activation pressures

At first, there was no idea to what extent the obstacles could still affect the flow field upon being pushed away from their initial position. Therefore, no further effect upon the

obstacles being moved was assumed, but the activation pressure of obstacles would be close to the pressure at the inception of their moving. A ±15% uncertainty of the friction coefficient was considered, then the values of 4.0×10^{-4}, 4.7×10^{-4} and 5.5×10^{-4} were applied to x_1, and 2.1×10^{-3}, 2.5×10^{-3} and 2.9×10^{-3} were applied to x_2. x_3 exhibited less uncertainty, hence, its value was considered as a constant (0.058 bar).

x_4 demonstrated the highest correlation with y_1, so the values close to y_1 (2.37) were denser with a small gradient, here 2.0, 2.45, 2.9, 4.5, 6.1 were applied to $x_{4,1}$. The random simulation results revealed that the highest overpressure in the tunnel was slightly higher (+0.3 bar or so) than the activation pressure of the steel slabs. To simulate the progressive failure process, each $x_{4,1}$ plus 0.1, 0.3, 0.5 was applied to $x_{4,44}$. For example, when $x_{4,1}$ was 2.0, $x_{4,44}$ was 2.1, 2.3, 2.5, respectively. The range of x_1, x_2, x_3, $x_{4,1}$, $x_{4,44}$ is presented in Table 5, and the corresponding values were applied in the numerical model to generate ANN input data.

Table 5 The range of x_1, x_2, x_3, $x_{4,1}$, $x_{4,44}$ (bar)

x_1	x_2	x_3	$x_{4,1}$	$x_{4,44}$
4.0×10^{-4}	2.1×10^{-3}		2.0	
4.7×10^{-4}	2.5×10^{-3}		2.45	
5.5×10^{-4}	2.9×10^{-3}	0.058	2.9	$x_{4,1}$+0.1, 0.3, 0.5
-	-		4.5	
-	-		6.1	

The simulation results are presented in Table 6, and the training and simulation results are illustrated in Fig. 17. A comparison between the numerical and ANN results indicates that the ANN-based tool has a good capability to fit the numerical data.

Table 6 The ANN input data

NO.	x_1 bar	x_2 bar	x_3 Bar	$x_{4,1}$ bar	$x_{1,44}$ bar	y_1 bar	y_2 Pa • s
1	4.7×10^{-4}	2.5×10^{-3}	0.058	4.50	4.60	4.72	68739
2	4.7×10^{-4}	2.5×10^{-3}	0.058	4.50	4.80	4.82	74290
3	4.7×10^{-4}	2.5×10^{-3}	0.058	4.50	5.00	4.84	77543
4	5.5×10^{-4}	2.1×10^{-3}	0.058	6.10	6.20	6.31	127846
5	5.5×10^{-4}	2.1×10^{-3}	0.058	6.10	6.40	6.34	130882
6	5.5×10^{-4}	2.1×10^{-3}	0.058	6.10	6.60	6.36	131975
7	4.0×10^{-4}	2.9×10^{-3}	0.058	2.00	2.10	2.26	31037
8	4.7×10^{-4}	2.5×10^{-3}	0.058	2.45	2.75	3.14	42337
9	4.7×10^{-4}	2.5×10^{-3}	0.058	2.45	2.95	3.24	43655
10	5.5×10^{-4}	2.1×10^{-3}	0.058	2.90	3.00	3.09	46685
11	5.5×10^{-4}	2.1×10^{-3}	0.058	2.90	3.20	3.30	49752
12	5.5×10^{-4}	2.1×10^{-3}	0.058	2.90	3.40	3.44	53320
13	4.7×10^{-4}	2.9×10^{-3}	0.058	6.10	6.20	6.09	128829
14	4.7×10^{-4}	2.9×10^{-3}	0.058	6.10	6.40	6.24	135113
15	4.7×10^{-4}	2.9×10^{-3}	0.058	6.10	6.60	6.24	137380

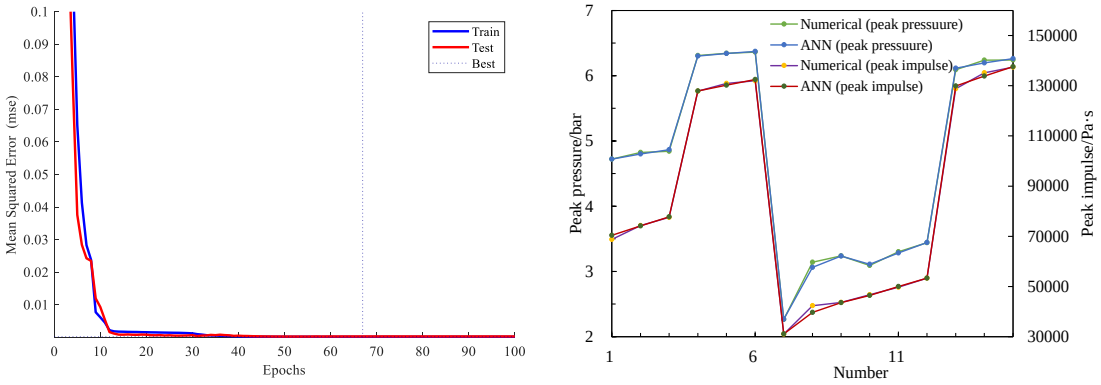

(a) The convergence curve (b) Comparison between numerical and ANN results

Fig. 17 ANN training result

In view of the trained network, a possible solution of x_1=4.5 × 10^{-4}, x_2=2.6 × 10^{-3}, x_3=0.058, $x_{4,1}$=2.0, $x_{4,44}$=2.3, $y_{1,ANN}$=2.76 and $y_{2,ANN}$=38079 was observed within the range of $x_1 \in (4.0 \times 10^{-4}, 6.0 \times 10^{-4})$, $x_2 \in (2.0 \times 10^{-3}, 3.0 \times 10^{-3})$, x_3=0.058, $x_{4,1} \in (1, 4)$ and $x_{4,44} \in (1.1, 4.5)$, and a total of 3×10^4 combinations were tested by the ANN network. Subsequently, this solution was tested through the numerical simulation. A comparison of ANN and numerical results are presented in Table 7. The deviation between the ANN and numerical results indicated the trained BP network had a good ability to predict the numerical results.

Table 7 The comparison of ANN and numerical results

Parameter	ANN	Numerical	error
y_1	2.76	2.56	7.9%
y_2	38079	36212	5.2%

A comparison of the numerical results with experimental data is depicted in Fig. 18. The peak pressure of △P2 predicted by the numerical model was observed to coincide with the experimental findings well, and the predicted peak impulse was close to the experimental data. However, the rate of pressure rise of the simulation result was slower as compared to the experimental findings.

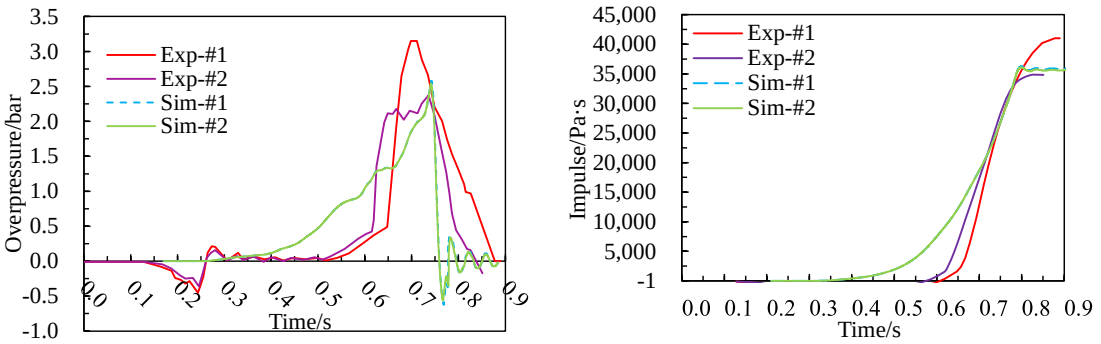

(a) Pressure history curve (b) Impulse curve

Fig. 18 The comparison between the numerical and experimental results

No further influence upon the obstacles being moved was assumed in this section, but the numerical model produced a lower rate of pressure rise which would lead to different structural responses (Caçoilo et al., 2021). In the experimental scenario, the obstacles still stayed in the tunnel for a while, which had an impact on the flow field upon being pushed away from their initial positions. Therefore, obstacles with larger activation pressures than calculated ones were studied to reveal to what extent these obstacles influenced the flow field upon being moved.

4.5.2 Obstacles with larger activation pressures than the calculated ones

The activation pressure of obstacles was increased to emulate their effect on the flow field after being moved, so x_1, x_2 were increased to as much as 5 times as their calculation values. The range of x_1, x_2, x_3, $x_{4,1}$, $x_{4,44}$ is presented in Table 8, and the corresponding values were applied to the numerical model to generate ANN input data.

Table 8 The range of x_1, x_2, x_3, $x_{4,1}$, $x_{4,44}$ (bar)

x_1	x_2	x_3	$x_{4,1}$	$x_{4,44}$
4.7×10^{-3}	2.5×10^{-3}		1.7	
1.4×10^{-3}	7.5×10^{-3}		2.0	
2.4×10^{-3}	1.3×10^{-2}	0.058	2.3	$x_{4,1}$+0.1, 0.3, 0.5
-	-		2.6	
-	-		2.9	

The simulation results are presented in Table 9, and the training and simulation findings are displayed in Fig. 19.

Table 9 The ANN input data

NO.	x_1 bar	x_2 bar	x_3 bar	$x_{4,1}$ bar	$x_{1,44}$ bar	y_1 bar	y_2 Pa • s
1	4.7×10^{-3}	2.5×10^{-3}	0.058	1.70	1.80	1.88	29353
2	4.7×10^{-3}	2.5×10^{-3}	0.058	1.70	2.00	2.08	32274
3	4.7×10^{-3}	2.5×10^{-3}	0.058	1.70	2.30	2.18	37409
4	2.4×10^{-3}	1.3×10^{-2}	0.058	2.30	2.40	3.24	19452
5	2.4×10^{-3}	1.3×10^{-2}	0.058	2.30	2.60	3.52	20230
6	2.4×10^{-3}	1.3×10^{-2}	0.058	2.30	2.80	3.89	21667
7	1.4×10^{-3}	2.5×10^{-3}	0.058	2.90	3.00	3.14	45541
8	1.4×10^{-3}	2.5×10^{-3}	0.058	2.90	3.20	3.41	48223
9	1.4×10^{-3}	2.5×10^{-3}	0.058	2.90	3.40	3.47	54950
10	1.4×10^{-3}	7.5×10^{-3}	0.058	2.00	2.1	2.49	19735
11	1.4×10^{-3}	7.5×10^{-3}	0.058	2.00	2.3	2.69	20675
12	1.4×10^{-3}	7.5×10^{-3}	0.058	2.00	2.5	2.94	21888
13	1.4×10^{-3}	1.3×10^{-2}	0.058	2.60	2.70	3.12	24220
14	1.4×10^{-3}	1.3×10^{-2}	0.058	2.60	2.90	3.43	25865
15	1.4×10^{-3}	1.3×10^{-2}	0.058	2.60	3.10	3.62	26926

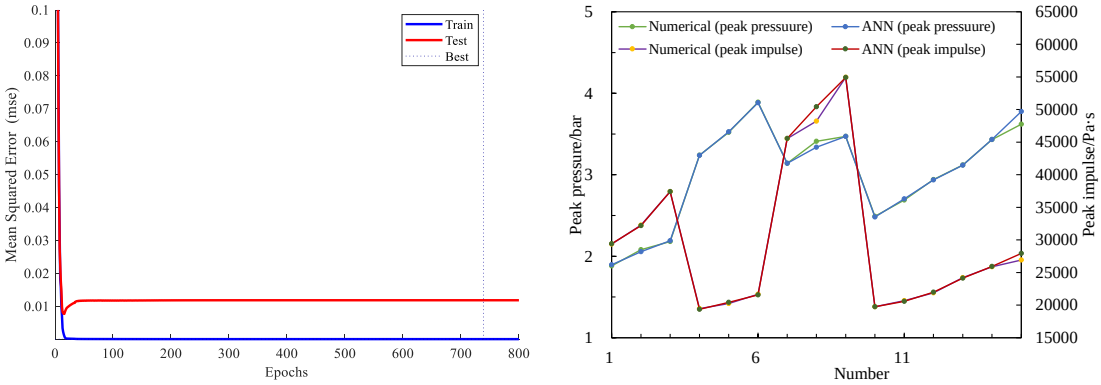

(a) The convergence curve (b) Comparison between numerical and ANN results

Fig. 19 ANN training results

Based on the trained network, a possible solution of x_1=1.2×10^{-3}, x_2=6.3×10^{-3}, x_3=0.058, $x_{4,1}$=2.30, $x_{4,44}$=2.85, $y_{1,\mathrm{ANN}}$=2.77 and $y_{2,\mathrm{ANN}}$=37934 was achieved within the range of x_1 ∈(4.7×10^{-4}, 2.4×10^{-3}), x_2∈(2.5×10^{-3}, 1.3×10^{-2}), x_3=0.058, $x_{4,1}$∈(1, 4) and $x_{4,44}$∈(1.1, 4.5), and a total of 66×10^4 combinations were tested by the ANN network. Afterwards, the solution was tested by the numerical model. The comparison of the ANN and numerical results is shown in Table 10.

Table 10 The comparison of ANN and numerical results

Parameter	ANN	Numerical	error
y_1	2.77	2.758	0.05%
y_2	37934	45137	-16.0%

The comparison between the numerical and experimental results is presented in Fig. 20 and Table 11. The history curves predicted by FLACS agreed well with the experimental ones. As seen in Fig. 21, the flame development from the tunnel gas vented explosion was projected in FLACS 3D view. In this simulation, the falling process of the steel slabs was not modeled. The determined x_1 and x_2 were 2.56 and 2.51 times as large as their calculated values, respectively, indicating their contribution to the flow field could not be ignored upon being pushed away from initial positions.

FLACS did not replicate the first overpressure peak of $\triangle P_1$ generated by the combination of gas combustion and gas escape from small gaps (Yang et al., 2021). These gaps were only several millimeters, whereas the numerical model was unable to mimic them since the grid resolution of 2 cm or less in explosion simulations is not recommended (Gexcon, 2019).

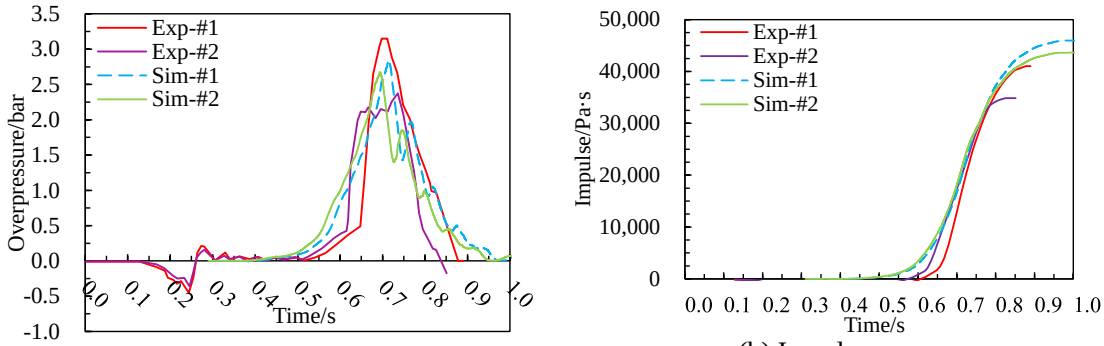

(a) Pressure history curve (b) Impulse curve

Fig. 20 The comparison between the numerical and experimental results

Table 11 The comparison of experimental and numerical results

Parameter	Experimental		Numerical	
	#1	#2	#1	#2
Peak pressure (bar)	3.15	2.37	2.84	2.67
Error	/	/	-9.8%	12.7%
Peak impulse (Pa·s)	41039	34868	46316	43959
Error	/	/	12.9%	26.1%

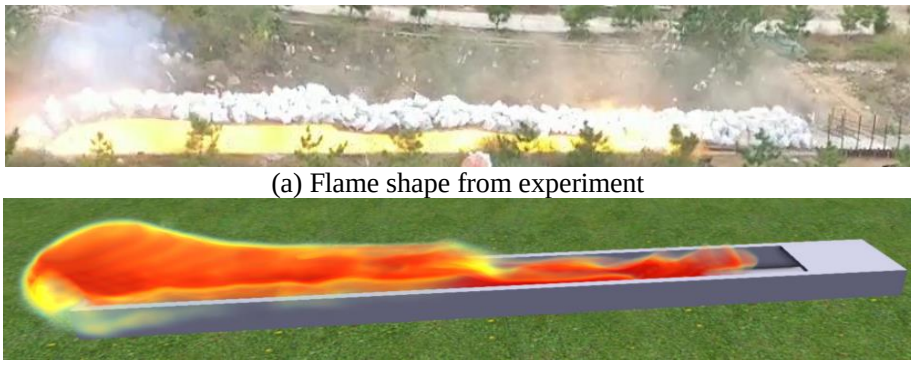

(a) Flame shape from experiment

(b) Flame shape from simulation

Fig. 21 Flame shape comparison

5 Conclusions

The modelling of a progressive vented gas explosion was presented using a CFD tool. Fixed vented gas explosion tests were used to validate the numerical model. The experimental results of a large-scale progressive vented gas explosion in a utility tunnel were utilized for further validation. A modified method based on a combination of the mathematical model and artificial neural network (ANN) was employed to help determine the critical parameters of the proposed model.

Generally, the numerical data matched with the experimental results. For the fixed vented gas explosion scenarios, the multiple overpressure peaks were predicted within satisfying error range by applying the first pressure peak as the activation pressure of the pressure relief panels, and the pressure history curves were roughly consistent with experimental

data. For the progressive vented gas explosion scenario, it was more challenging to replicate the experimental results owing to its complex boundary conditions. The method which was suitable for fixed vented gas explosion to estimate the activation pressure of the pressure relief panels underestimated the overpressure for the progressive vented gas explosion. According to the correlation analysis among the activation pressure of the pressure relief panels and peak pressure as well as peak impulse, the vent covers had an insignificant impact on the gas explosion load after being lifted over the tunnel top. The falling process of the vent covers was not necessary to be modelled. The progressive vented gas explosion process could be modelled by two-layer pressure relief panels with the activation pressures of the upper layer having a linear ascent trend from the ignition end to the other end. The activation pressures of obstacles inside the tunnel were about 2.5 times as large as their calculated value, indicating the obstacles' contribution to the flow field could not be ignored upon being pushed away from initial positions. An ANN-based tool was utilized to help determine the critical parameters in the numerical model, so as to save computational time involved in pure numerical simulation.

Acknowledgements

This work was supported by the Australia Research Council under ARC Discovery Project DP210101100.

References

Arntzen, B.J., 1998. Modelling of turbulence and combustion for simulation of gas explosions in complex geometries. Dr. Ing. Thesis., https://ntnuopen.ntnu.no/ntnu-xmlui/bitstream/handle/11250/227921/122240_FULLTEXT01.pdf?sequence=1&isAllowed=y.

Bakke, J.R., Skogrand, P.E., Asa, A.K., 2004. Explosion Relief Panels and Their Effect on Gas Explosion Overpressure. 1-8, http://doi.org/10.1115/OMAE2004-51005.

Bleyer, A., Taveau, J., Djebaïli-Chaumeix, N., Paillard, C.E., Bentaïb, A., 2012. Comparison between FLACS explosion simulations and experiments conducted in a PWR Steam Generator casemate scale down with hydrogen gradients. Nucl. Eng. Des. 245, 189-196, http://doi.org/10.1016/j.nucengdes.2012.01.010.

BP, P.L.C., 2021. Statistical Review of World Energy. https://www.bp.com/content/dam/bp/business-sites/en/global/corporate/pdfs/energy-economics/statistical-review/bp-stats-review-2021-full-report.pdf.

Caçoilo, A., Mourão, R., Teixeira-Dias, F., Lecompte, D., Rush, D., 2021. Structural response of corrugated plates under blast loading: The influence of the pressure-time history. Structures 30, 531-545, http://doi.org/10.1016/j.istruc.2021.01.025.

Cheng, L., Li, S., Ma, L., Li, M., Ma, X., 2015. Fire spread simulation using GIS: Aiming at urban natural gas pipeline. Safety Sci. 75, 23-35, http://doi.org/10.1016/j.ssci.2015.01.002.

Chmielewski, R., Bąk, A., 2021. Analysis of the safety of residential buildings under gas explosion loads. Journal of Building Engineering 43, 102815, http://doi.org/10.1016/j.jobe.2021.102815.

Cooper, M.G., Fairweather, M., Tite, J.P., 1986. On the Mechanisms of Pressure Generation in Vented Explosions. Combust. Flame 1, 1-14, http://doi.org/10.1016/0010-2180(86)90067-2.

Department Of Defense, 2008. Structures To Resist The Effects Of Accidental Explosions. https://www.wbdg.org/ffc/dod/unified-facilities-criteria-ufc/ufc-3-340-02

Pressure relief panel failure pressure prediction, 2022. https://github.com/DearChen6666/pressure-relief-panel-failure-pressure-prediction

European Committee for Standardization., 2007. Gas explosion venting protective systems. https://cdn.standards.iteh.ai/samples/14897/d43645766c484520bca5b8ea2f9436b0/SIST-EN-14994-2007.pdf

Fu, T., Tang, X., Cai, Z., Zuo, Y., Tang, Y., Zhao, X., 2020. Correlation research of phase angle variation and coating performance by means of Pearson's correlation coefficient. Prog. Org. Coat. 139, 105459, http://doi.org/10.1016/j.porgcoat.2019.105459.

Gexcon, 2019. FLACS v10.9 User's Manual.

Guo, J., Wang, C., Li, Q., Chen, D., 2016. Effect of the vent burst pressure on explosion venting of rich methane-air mixtures in a cylindrical vessel. J. Loss Prevent. Proc. 40, 82-88, http://doi.org/10.1016/j.jlp.2015.12.006.

Jaaranen, J., Fink, G., 2020. Frictional behaviour of timber-concrete contact pairs. Constr. Build. Mater. 243, 118273, http://doi.org/10.1016/j.conbuildmat.2020.118273.

Kasmani, R.M., Andrews, G.E., Phylaktou, H.N., 2013. Experimental study on vented gas explosion in a cylindrical vessel with a vent duct. Process Saf. Environ. 91, 245-252, http://doi.org/10.1016/j.psep.2012.05.006.

Kumar, A., 1994. Guidelines for Evaluating the Characteristics of Vapor Cloud Explosions, Flash Fires, and BLEVEs, American Institute of Chemical Engineers, New York, USA.

Launder, B.E., Spalding, D.B., 1974. The numerical computation of turbulent flows. Comput. Method. Appl. M. 3, 269–289, http://doi.org/10.1016/b978-0-08-030937-8.50016-7 .

Li, F.G., Chen, L., 2014. Gas Explosion Effect on Structure Damage and Control Measures. Applied Mechanics and Materials 501-504, 2424-2427, http://doi.org/10.4028/www.scientific.net/AMM.501-504.2424.

Li, J., Cheng, J., Shi, J., Huang, F., 2012.Brief Introduction of Back Propagation (BP) Neural Network Algorithm and Its Improvement, in:(Eds.),Springer Berlin Heidelberg, Berlin, Heidelberg, pp. 553-558.

Li, J., Hao, H., 2018. Far-field pressure prediction of a vented gas explosion from storage tanks by using new CFD simulation guidance. Process Saf. Environ. 119, 360-378, http://doi.org/10.1016/j.psep.2018.08.004.

Li, J., Hao, H., 2019. Numerical and analytical prediction of pressure and impulse from vented gas explosion in large cylindrical tanks. Process Saf. Environ. 127, 226-244, http://doi.org/10.1016/j.psep.2019.05.019.

Li, J., Hernandez, F., Hao, H., Fang, Q., Xiang, H., Li, Z., Zhang, X., Chen, L., 2017. Vented Methane-air Explosion Overpressure Calculation—A simplified approach based on CFD. Process Saf. Environ. 109, 489-508, http://doi.org/10.1016/j.psep.2017.04.025.

[a]Li, Z., Chen, L., Fang, Q., Chen, W., Hao, H., Zhang, Y., 2017. Experimental and numerical study of basalt fiber reinforced polymer strip strengthened autoclaved aerated concrete masonry walls under vented gas explosions. Eng. Struct. 152, 901-919, http://doi.org/10.1016/j.engstruct.2017.09.055.

[b]Li, Z., Chen, L., Fang, Q., Chen, W., Hao, H., Zhu, R., Zheng, K., 2019. Experimental and numerical study on CFRP strip strengthened clay brick masonry walls subjected to vented gas explosions. Int. J. Impact Eng. 129, 66-79, http://doi.org/10.1016/j.ijimpeng.2019.02.013.

[c]Li, Z., Chen, L., Fang, Q., Hao, H., Zhang, Y., Chen, W., Xiang, H., Bao, Q., 2017. Study of autoclaved aerated concrete masonry walls under vented gas explosions. Eng. Struct. 141, 444-460, http://doi.org/10.1016/j.engstruct.2017.03.033.

[d]Li, Z., Chen, L., Fang, Q., Hao, H., Zhang, Y., Xiang, H., Chen, W., Yang, S., Bao, Q., 2017. Experimental and numerical study of unreinforced clay brick masonry walls subjected to vented gas explosions. Int. J. Impact Eng. 104, 107-126, http://doi.org/10.1016/j.ijimpeng.2017.02.002.

Lucas, M., Atanga, G., Hisken, H., Mauri, L., Skjold, T., 2021. Simulating vented hydrogen deflagrations: Improved modelling in the CFD tool FLACS-hydrogen. Int. J. Hydrogen Energ. 46, 12464-12473, http://doi.org/10.1016/j.ijhydene.2020.09.073.

Meng, Q., Wu, C., Hao, H., Li, J., Wu, P., Yang, Y., Wang, Z., 2020. Steel fibre reinforced alkali-activated geopolymer concrete slabs subjected to natural gas

explosion in buried utility tunnel. Constr. Build. Mater. 246, 118447, http://doi.org/10.1016/j.conbuildmat.2020.118447.

[a]Meng, Q., Wu, C., Li, J., Liu, Z., Wu, P., Yang, Y., Wang, Z., 2020. Steel/basalt rebar reinforced Ultra-High Performance Concrete components against methane-air explosion loads. Composites Part B: Engineering 198, 108215, http://doi.org/10.1016/j.compositesb.2020.108215.

[b]Meng, Q., Wu, C., Li, J., Liu, Z., Wu, P., Yang, Y., Wang, Z., 2020. Steel/basalt rebar reinforced Ultra-High Performance Concrete components against methane-air explosion loads. Composites Part B: Engineering 198, 108215, http://doi.org/10.1016/j.compositesb.2020.108215.

Meng, Q., Wu, C., Li, J., Wu, P., Xu, S., Wang, Z., 2021. A study of pressure characteristics of methane explosion in a 20 m buried tunnel and influence on structural behaviour of concrete elements. Eng. Fail. Anal. 122, 105273, http://doi.org/10.1016/j.engfailanal.2021.105273.

National Fire Protection Association, 2007. Standard on Explosion Protection by Deflagration Venting. https://www.nfpa.org/codes-and-standards/all-codes-and-standards/list-of-codes-and-standards/detail?code=68

Nishimura, I., Mogi, T., Dobashi, R., 2013. Simple method for predicting pressure behavior during gas explosions in confined spaces considering flame instabilities. J. Loss Prevent. Proc. 26, 351-354, http://doi.org/10.1016/j.jlp.2011.08.009.

Park, D.J., Lee, Y.S., Green, A.R., 2008. Experiments on the effects of multiple obstacles in vented explosion chambers. J. Hazard. Mater. 153, 340-350, http://doi.org/10.1016/j.jhazmat.2007.08.055.

Pedersen, H.H., Middha, P., 2012. Modelling of Vented Gas Explosions in the CFD tool FLACS. Chemical engineering transactions 26, http://doi.org/10.3303/CET1226060.

Pedersen, H.H., Tomlin, G., Middha, P., Phylaktou, H.N., Andrews, G.E., 2013. Modelling large-scale vented gas explosions in a twin-compartment enclosure. J. Loss Prevent. Proc. 26, 1604-1615, http://doi.org/10.1016/j.jlp.2013.08.001.

Rabbat, B.G., Asce, M., Russell, H.G., 1985. Friction Coefficient of Steel on Concrete or Grout. J. Struct. Eng. 111, 505-515, http://doi.org/10.1061/(ASCE)0733-9445(1985)111:3(505).

Salaun, N., Arve, G.H., Per, E.N., 2016. Risk-based Structural Response against Explosion Blast Loads: Systematic One-to-one CFD (FLACS) / NLFEA (Impetus Afea solver) Coupling to Derive Quantified Response Exceedance. Chemical engineering transactions 48, http://doi.org/10.3303/CET1648010.

Tolias, I.C., Giannissi, S.G., Venetsanos, A.G., Keenan, J., Shentsov, V., Makarov, D., Coldrick, S., Kotchourko, A., Ren, K., Jedicke, O., Melideo, D., Baraldi, D., Slater, S., Duclos, A., Verbecke, F., Molkov, V., 2019. Best practice guidelines in

numerical simulations and CFD benchmarking for hydrogen safety applications. Int. J. Hydrogen Energ. 44, 9050-9062, http://doi.org/10.1016/j.ijhydene.2018.06.005.

Tomlin, G., Johnson, D.M., Cronin, P., Phylaktou, H.N., Andrews, G.E., 2015. The effect of vent size and congestion in large-scale vented natural gas/air explosions. J. Loss Prevent. Proc. 35, 169-181, http://doi.org/10.1016/j.jlp.2015.04.014.

Vyazmina, E., Jallais, S., 2016. Validation and recommendations for FLACS CFD and engineering approaches to model hydrogen vented explosions: Effects of concentration, obstruction vent area and ignition position. Int. J. Hydrogen Energ. 41, 15101-15109, http://doi.org/10.1016/j.ijhydene.2016.05.189.

Wang, Q., Luo, X., Wang, C., Liu, Y., Zhou, P., Li, B., 2022. Experimental study on external explosion for vented hydrogen deflagration in a rectangular tube with different vent coefficients. Process Saf. Environ. 158, 331-339, http://doi.org/10.1016/j.psep.2021.12.002.

Xing, H., Xu, Q., Song, X., Wang, Y., Li, B., Xie, L., 2020. The effects of vent area and ignition position on pressure oscillations in a large L/D ratio duct. Process Saf. Environ. 135, 166-170, http://doi.org/10.1016/j.psep.2019.12.030.

Yang, H., Chen, J., Chiu, H., Kao, T., Tsai, H., Chen, J., 2016. Confined vapor explosion in Kaohsiung City – A detailed analysis of the tragedy in the harbor city. J. Loss Prevent. Proc. 41, 107-120, http://doi.org/10.1016/j.jlp.2016.03.017.

Yang, Y., Wu, C., Liu, Z., Du, J., Zhang, H., Xu, S., Zhou, S., 2021. Protective effect of unbonded prestressed ultra-high performance reinforced concrete slab against gas explosion in buried utility tunnel. Process Saf. Environ. 149, 370-384, http://doi.org/10.1016/j.psep.2020.11.002.

Yu, M., Wan, S., Zheng, K., Guo, P., Chu, T., Yuan, Z., 2017. Influence on the methane/air explosion characteristics of the side venting position in a pipeline. Process Saf. Environ. 111, 292-299, http://doi.org/10.1016/j.psep.2017.07.017.

Zhu, Y., Qian, X., Liu, Z., Huang, P., Yuan, M., 2015. Analysis and assessment of the Qingdao crude oil vapor explosion accident: Lessons learnt. J. Loss Prevent. Proc. 33, 289-303, http://doi.org/10.1016/j.jlp.2015.01.004.

Zhu, Y., Wang, D., Shao, Z., Zhu, X., Xu, C., Zhang, Y., 2020. Investigation on the overpressure of methane-air mixture gas explosions in straight large-scale tunnels. Process Saf. Environ. 135, 101-112, http://doi.org/10.1016/j.psep.2019.12.022.